DUST AND GAS IN THE MAGELLANIC CLOUDS FROM THE HERITAGE *HERSCHEL* KEY PROJECT. I. DUST PROPERTIES AND INSIGHTS INTO THE ORIGIN OF THE SUBMILLIMETER EXCESS EMISSION[*]

Karl D. Gordon[1,2], Julia Roman-Duval[1], Caroline Bot[3], Margaret Meixner[1], Brian Babler[4],
Jean-Philippe Bernard[5,6], Alberto Bolatto[7], Martha L. Boyer[8,9], Geoffrey C. Clayton[10], Charles Engelbracht[11,12],
Yasuo Fukui[13], Maud Galametz[14], Frederic Galliano[15], Sacha Hony[15], Annie Hughes[16], Remy Indebetouw[17],
Frank P. Israel[18], Katherine Jameson[7], Akiko Kawamura[19], Vianney Lebouteiller[15], Aigen Li[20], Suzanne
C. Madden[15], Mikako Matsuura[21], Karl Misselt[11], Edward Montiel[10,11], K. Okumura[15], Toshikazu Onishi[22],
Pasquale Panuzzo[15,23], Deborah Paradis[5,6], Monica Rubio[24], Karin Sandstrom[11], Marc Sauvage[15],
Jonathan Seale[1,25], Marta Sewiło[25], Kirill Tchernyshyov[25], and Ramin Skibba[11,26]
[1] Space Telescope Science Institute, 3700 San Martin Drive, Baltimore, MD 21218, USA
[2] Sterrenkundig Observatorium, Universiteit Gent, Krijgslaan 281, B-9000 Gent, Belgium
[3] Observatoire astronomique de Strasbourg, Université de Strasbourg, CNRS, UMR 7550, 11 rue de l Université, F-67000 Strasbourg, France
[4] Department of Astronomy, 475 North Charter Street, University of Wisconsin, Madison, WI 53706, USA
[5] CESR, Université de Toulouse, UPS, 9 Avenue du Colonel Roche, F-31028 Toulouse, Cedex 4, France
[6] Université de Toulouse, UPS-OMP, IRAP, F-31028 Toulouse Cedex 4, France
[7] Department of Astronomy, Lab for Millimeter-wave Astronomy, University of Maryland, College Park, MD 20742-2421, USA
[8] Observational Cosmology Lab, Code 665, NASA Goddard Space Flight Center, Greenbelt, MD 20771, USA
[9] Oak Ridge Associated Universities (ORAU), Oak Ridge, TN 37831, USA
[10] Department of Physics and Astronomy, Louisiana State University, 233-A Nicholson Hall, Tower Drive, Baton Rouge, LA 70803, USA
[11] Steward Observatory, University of Arizona, 933 North Cherry Avenue, Tucson, AZ 85721, USA
[12] Raytheon Company, 1151 East Hermans Road, Tucson, AZ 85756, USA
[13] Department of Physics, Nagoya University, Furo-cho, Chikusa-ku, Nagoya 464-8602, Japan
[14] European Southern Observatory, Karl-Schwarzschild-Str. 2, D-85748 Garching-bei-Mnchen, Germany
[15] CEA, Laboratoire AIM, Irfu/SAp, Orme des Merisiers, F-91191 Gif-sur-Yvette, France
[16] Max-Planck-Institut für Astronomie, Königstuhl 17, D-69117 Heidelberg, Germany
[17] Department of Astronomy, University of Virginia, and National Radio Astronomy Observatory, 520 Edgemont Road, Charlottesville, VA 22903, USA
[18] Sterrewacht Leiden, Leiden University, P.O. Box 9513, NL-2300 RA Leiden, The Netherlands
[19] National Astronomical Observatory of Japan, Osawa, Mitaka, Tokyo, 181-8588, Japan
[20] 314 Physics Building, Department of Physics and Astronomy, University of Missouri, Columbia, MO 65211, USA
[21] Department of Physics and Astronomy, University College London, Gower Street, London WC1E 6BT, UK
[22] Department of Astrophysics, Graduate School of Science, Osaka Prefecture University, Sakai, Osaka 599-8531, Japan
[23] CNRS, Observatoire de Paris-Lab. GEPI, Bat. 11, 5, place Jules Janssen, F-92195 Meudon CEDEX, France
[24] Departamento de Astronomía, Universidad de Chile, Casilla 36-D, Santiago, Chile
[25] Department of Physics and Astronomy, The Johns Hopkins University, 366 Bloomberg Center, 3400 North Charles Street, Baltimore, MD 21218, USA
[26] Center for Astrophysics and Space Sciences, Department of Physics, University of California, 9500 Gilman Drive, La Jolla, San Diego, CA 92093, USA

ABSTRACT

The dust properties in the Large and Small Magellanic clouds (LMC/SMC) are studied using the HERITAGE *Herschel* Key Project photometric data in five bands from 100 to 500 μm. Three simple models of dust emission were fit to the observations: a single temperature blackbody modified by a power-law emissivity (SMBB), a single temperature blackbody modified by a broken power-law emissivity (BEMBB), and two blackbodies with different temperatures, both modified by the same power-law emissivity (TTMBB). Using these models, we investigate the origin of the submillimeter excess, defined as the submillimeter emission above that expected from SMBB models fit to observations $<200\,\mu$m. We find that the BEMBB model produces the lowest fit residuals with pixel-averaged 500 μm submillimeter excesses of 27% and 43% for the LMC and SMC, respectively. Adopting gas masses from previous works, the gas-to-dust ratios calculated from our fitting results show that the TTMBB fits require significantly more dust than are available even if all the metals present in the interstellar medium (ISM) were condensed into dust. This indicates that the submillimeter excess is more likely to be due to emissivity variations than a second population of colder dust. We derive integrated dust masses of $(7.3 \pm 1.7) \times 10^5$ and $(8.3 \pm 2.1) \times 10^4\,M_\odot$ for the LMC and SMC, respectively. We find significant correlations between the submillimeter excess and other dust properties; further work is needed to determine the relative contributions of fitting noise and ISM physics to the correlations.

Key words: infrared: galaxies – infrared: ISM – ISM: general – Magellanic clouds

Online-only material: color figures

1. INTRODUCTION

Among nearby galaxies, the Large Magellanic cloud (LMC) and Small Magellanic cloud (SMC) represent unique astrophysical laboratories for interstellar medium (ISM) studies. Both clouds are relatively nearby, the LMC at ∼50 kpc (Walker 2012)

---

and the SMC at ∼60 kpc (Hilditch et al. 2005), and provide ISM measurements that are relatively unconfused along the line of sight as compared to similar observations in the Milky Way (MW). The LMC and SMC ultraviolet dust extinction properties show strong variations both internally and in global averages in comparison to each other and the MW (Lequeux et al. 1982; Prevot et al. 1984; Clayton & Martin 1985; Fitzpatrick 1985; Gordon et al. 2003; Maíz Apellániz & Rubio 2012). The two clouds span an important metallicity range with the LMC at ∼1/2 $Z_\odot$ (Russell & Dopita 1992) being above and the SMC at ∼1/5 $Z_\odot$ (Russell & Dopita 1992) being below the threshold of one-third to one-fourth $Z_\odot$ where the properties of the ISM change significantly as traced by the reduction in the polycyclic aromatic hydrocarbon (PAH) dust mass fractions and (possibly) dust-to-gas ratios (Draine et al. 2007). The far-infrared (FIR) to submillimeter emission from the clouds shows more submillimeter emission than expected from existing dust grain models, with the SMC having a larger amount of this excess emission (Israel et al. 2010; Bot et al. 2010b).

The submillimeter excess was seen first in the MW using the COBE/FIRAS (Boggess et al. 1992; Mather et al. 1993) observations of high-latitude cirrus dust emission (Wright et al. 1991; Reach et al. 1995). These works found that the 100–300 μm observations were well modeled with a single temperature blackbody modified with a power-law emissivity, but that the longer wavelength observations ($\lambda > 300\,\mu$m) required a second dust component with a temperature of 4–7 K. The spatial correlation of this second dust component with the hotter main dust component along with physical arguments on dust heating led Reach et al. (1995) to argue that emissivity variations away from a simple power law were more likely to explain the observations than a second component of very cold dust. The need for a nontrivial FIR to submillimeter dust emissivity shape was quantified by Li & Draine (2001), where they modified the emissivity of "astronomical" silicate grains to have an emissivity with a shallower wavelength dependence at $\lambda > 200\,\mu$m than at $\lambda < 200\,\mu$m. More recently, Paradis et al. (2012) analyzed *Herschel Space Observatory* (Pilbratt et al. 2010) observations of the MW plane and found a significant submillimeter excess at 500 μm that increased from the inner to the outer Galaxy.

Previous work on the submillimeter excess in nearby galaxies by Galliano et al. (2003, 2005) and Galametz et al. (2011) used the combination of FIR observations ($\lambda < 200\,\mu$m) from the *Infrared Space Observatory* (Kessler et al. 1996) and *Spitzer Space Telescope* (Werner et al. 2004) with submillimeter observations ($\lambda \sim 850\,\mu$m) taken using ground-based observatories. These works provided strong evidence of a submillimeter excess at ∼850 μm and that this excess is the largest in low metallicity galaxies. With the advent of *Herschel* observations, the presence of a submillimeter excess at 500 μm has been established in many low metallicity galaxies including the Magellanic clouds (Gordon et al. 2010; Meixner et al. 2010; Galliano et al. 2011; Dale et al. 2012; Kirkpatrick et al. 2013; Rémy-Ruyer et al. 2013).

The definition of the submillimeter excess has not been uniformly defined in the literature, complicating the comparisons between different studies. Generally, a model is used to define the zero submillimeter excess baseline; this model varies from simple modified blackbodies to more complex dust grain models. In addition, the uncertainties assumed on the observations have varied leading to the same submillimeter excess level being considered significant by one work and not significant by another. This illustrates the need for a uniform definition of reference spectral energy distribution (SED) from which to measure the submillimeter excess and a common set of assumptions on the observational uncertainties. It is also critically important to properly include the full observational uncertainties, both correlated and uncorrelated, as shown by Galliano et al. (2011) and Veneziani et al. (2013).

For clarity in this paper, we adopt the definition of the submillimeter excess as the excess emission seen at submillimeter wavelengths above that expected for dust grains with a single temperature and a $\lambda^{-\beta_{\rm eff}}$ emissivity law. This simple model is used to fit an observed SED, with the value of $\beta_{\rm eff}$ providing a measure of the effective emissivity law. The origin of the observed effective emissivity law variations may be due to one or a combination of factors including intrinsic dust emissivity variations, mixing of different dust compositions, and variations in dust temperatures along the line of sight.

Laboratory studies of the two main interstellar dust analogs have shown that carbonaceous grains have $\beta \sim 1$–2 (Mennella et al. 1995; Zubko et al. 1996; Jager et al. 1998) and silicate grains have $\beta \sim 2$ (Mennella et al. 1998; Boudet et al. 2005; Coupeaud et al. 2011) in the FIR and submillimeter wavelength range. The value of $\beta_{\rm eff}$ for a mixed composition dust population is determined by both the actual ratio of the two compositions and the spectral shape of the heating radiation field. Silicate and carbonaceous grains have significantly different ultraviolet/optical absorption properties and any change in the radiation field spectrum will change the luminosity weighting present in the infrared (IR) dust emission SED. Deviations from simple $\lambda^{-\beta}$ emissivity laws and dependence on temperature are seen in laboratory work on dust analogs, with silicate grains having larger such variations than carbonaceous grains (Mennella et al. 1998; Boudet et al. 2005; Coupeaud et al. 2011). Such deviations have already been seen in astronomical observations, leading Li & Draine (2001) to modify their model of "astronomical" silicates such that it already includes a submillimeter excess of 11% at 500 μm, according to our definition above. Similar broken power-law dust emissivities have been implied by FIR to submillimeter observations of the different phases of the MW ISM (Paradis et al. 2009).

Multiple dust temperatures along the line of sight can also cause effective emissivity law variations. The simplest case to consider is two dust populations with the second population having a significantly colder temperature than the first. Fitting the composite SED of this dust with a single temperature $\lambda^{-\beta_{\rm eff}}$ emissivity law model will result in a submillimeter excess at the wavelengths where the second cold dust population contributes. Such two temperature models have been studied by Juvela & Ysard (2012) who find that the $\beta_{\rm eff}$ can either be higher or lower than the intrinsic β depending the distribution of temperatures. More complex temperature mixing has been investigated with similar results (Shetty et al. 2009a, 2009b; Juvela & Ysard 2012; Ysard et al. 2012).

The implications for our understanding of dust grain properties are quite different depending on the origin of the submillimeter excess. If the submillimeter excess is due to very cold dust, then the total dust mass would potentially increase significantly as a large mass of cold dust is needed to reproduce the observed emission (e.g., Galliano et al. 2005). On the other hand, if the submillimeter excess is due to dependencies of the effective emissivity law with wavelength, then this provides insights into variations in the ratio of silicate/carbonaceous grains and/or variations in spectral shape of the illuminating radiation field.

The Magellanic clouds provide two of the best laboratories to study the submillimeter excess given their proximity and lower than MW metallicities. Work on this topic in the Magellanic clouds prior to the *Herschel* observations has used ground-based submillimeter observations (e.g., Bot et al. 2010a) or low spatial resolution PLANCK observations. In particular, the studies by Israel et al. (2010) and Bot et al. (2010b) clearly show a submillimeter excess in both clouds, even though the works were focused on the longer wavelength emission of the clouds. They found that the observed submillimeter excess can be explained using Draine & Li (2007) models with cold dust grains, but not by emission due to spinning grains, which is the likely origin of the excess emission they observed at millimeter to centimeter wavelengths. Similar results for the submillimeter excess in the SMC were found using the PLANCK observations (Planck Collaboration et al. 2011; C. Verdugo et al. in preparation). In apparent conflict with these wide-field and/or global studies of dust emission in the clouds, a spatially resolved study by Galametz et al. (2013) found no evidence for a submillimeter excess at 870 μm in N159, a massive star-forming complex in the LMC. As noted by the authors, however, their conclusions apply only to high surface brightness regions that can be detected using ground-based submillimeter observations.

The HERschel Inventory of The Agents of Galaxy Evolution (HERITAGE) in the Magellanic clouds *Herschel* Key Project has mapped both clouds providing observations at 100, 160, 250, 350, and 500 μm (Meixner et al. 2013). The HERITAGE wavelength coverage (100–500 μm) and spatial resolution ($\sim$10 pc at 500 μm) are well suited for measuring the spatial variations of dust properties probed by FIR and submillimeter emission. In particular, these observations are ideally suited to investigating the nature of the submillimeter excess and how it varies spatially in each cloud. The HERITAGE project test observations of a strip in the LMC have been analyzed and a measurable submillimeter excess at 500 μm was found using both simple single temperature blackbodies (Gordon et al. 2010) and a more complex dust grain model (Meixner et al. 2010; Galliano et al. 2011). These studies found that this submillimeter excess was anti-correlated with ISM (gas or dust) surface density.

The goal of this paper is to investigate the submillimeter excess in both Magellanic clouds using the full HERITAGE data using simple dust emission models based on one or two modified blackbodies. We choose to use such models for this paper since they allow large potential variations in the effective emissivity laws, whereas existing dust grain models do not incorporate the full range of variations indicated by laboratory studies of ISM dust analogs. In addition, we are careful to use a robust model of the uncertainties in the measurements, including the correlations between the different *Herschel* bands due to the absolute flux calibration and the background subtraction. Preliminary versions of the dust surface density maps derived in this paper were used to study the correlation between dust and stellar properties in the Magellanic clouds by Skibba et al. (2012).

2. DATA

The FIR and submillimeter observations of the Magellanic clouds analyzed in this study were taken as part of the HERITAGE Key Project (Meixner et al. 2013) using the PACS (Poglitsch et al. 2010) and SPIRE (Griffin et al. 2010) instruments on the *Herschel Space Observatory*. The observations provided images of the LMC and SMC at 100, 160, 250, 350, and 500 μm that cover the entire IR emitting regions of both galaxies (8°×8°.5 and 5°×5° + 4°×3° for the LMC and SMC, respectively). The observation and data reduction details can be found in Meixner et al. (2013). It is useful to note that as part of the data reduction, the *IRAS* 100 μm (Schwering & Israel 1989; Schwering 1989) and MIPS 160 μm images (Meixner et al. 2006; Gordon et al. 2011) for each galaxy were used to correct for the drifting baseline of the PACS bolometers. Thus the PACS 100 and 160 μm images contain the *IRAS* 100 and MIPS 160 information as well as the new PACS observations.

Additional processing steps were performed for this study to create images that had the same spatial resolution and the same foreground/background subtraction. First, each image was convolved with a kernel that transformed the spatial resolution of the images to the lowest resolution of the set of images, set by the SPIRE 500 μm point-spread function (PSF) which has a resolution of $\sim$40″. The Aniano et al. (2011) convolution kernels were used for this step as they directly and optimally transform the native PSF to that of the SPIRE 500 μm PSF.

Second, a foreground subtraction was done to remove the structured emission due to MW dust (cirrus) emission. The detailed structure of the MW dust emission in the PACS and SPIRE bands was predicted using the integrated MW velocity H I gas maps in the direction of the LMC (Staveley-Smith et al. 2003) and SMC (Stanimirović et al. 2000; Muller et al. 2003) and the Desert et al. (1990) model for the local interstellar radiation field. This model gives the conversion between the H I column and infrared emission. The conversion coefficients used were 1.073, 1.848, 1.202, 0.620, and 0.252 (MJy sr^{-1}) (1 × 10^{20} H I atoms/cm^2)$^{-1}$ for 100, 160, 250, 350, and 500 μm, respectively. These conversion coefficients are higher than those that would be obtained with the newer DustEM model (Compiègne et al. 2011) for the same radiation field, but are similar to the observed correlations between the MW velocity integrated H I and the diffuse emission measured in the same bands in regions outside of the SMC. This step was particularly important for the SMC where structures with similar surface brightnesses to those in the galaxy were removed by this subtraction.

Finally, a residual large scale structure in the background was removed using a low order two-dimensional surface polynomial interpolation that was constrained by regions external to each galaxy. The baseline subtraction reduction step for PACS and SPIRE data used different assumptions for these external regions (Meixner et al. 2013) and, thus, this final step ensures that all the images have the same background subtraction. This background subtraction is especially important for the LMC where the SPIRE observations included emission near the edges of the HERITAGE coverage due to the very extended nature of the LMC (especially south of the LMC main body) and the excellent sensitivity of the SPIRE instrument.

3. MODELS

We use three different models to fit the FIR/submillimeter surface brightness measurements. The first model is a single temperature blackbody modified by a single power-law emissivity (SMBB). The second model assumes that the submillimeter excess emission is due to variations in the wavelength dependence of the dust emissivity law that is parameterized by a broken power law (BEMBB). The third model assumes that the submillimeter excess emission is due to a second, lower temperature population of dust grains (TTMBB). All of our models assume equilibrium heating only and thus we restrict

our fits to using only data $\geqslant 100\,\mu$m. It is reasonable to expect that the emission at these wavelengths is dominated by equilibrium emission from dust grains. In this analysis, any residual $100\,\mu$m contribution due to emission from transitionally heated grains will yield a somewhat higher dust temperature (and thus a smaller dust column density) than would be found with our models. In the great majority of sight lines, this contribution is too small to be of concern, but may introduce a systematic bias in the regions near intense star formation.

In general, the surface brightness of dust with temperature, T_d, is

$$S_\lambda = \tau_\lambda B_\lambda(T_d) \tag{1}$$

$$= N_d \pi a^2 Q_\lambda B_\lambda(T_d) \tag{2}$$

$$= \frac{\Sigma_d}{m_d} \pi a^2 Q_\lambda B_\lambda(T_d) \tag{3}$$

$$= \frac{\Sigma_d}{\frac{4}{3} a^3 \rho} \pi a^2 Q_\lambda B_\lambda(T_d) \tag{4}$$

$$= \frac{3}{4a\rho} \Sigma_d Q_\lambda B_\lambda(T_d) \tag{5}$$

$$= \kappa_\lambda \Sigma_d B_\lambda, \tag{6}$$

where τ_λ is the dust optical depth, N_d is the dust column density, a is the grain radius, Q_λ is the dust emissivity, B_λ is the Planck function, Σ_d is the dust surface mass density, m_d is the mass of a single dust grain, ρ is the grain density, κ_λ is the grain absorption cross section per unit mass. These equations can be evaluated in standards units (e.g., cgs or MKS). We found it convenient to express Σ_d in $M_\odot\,\mathrm{pc}^{-2}$, κ_λ in $\mathrm{cm}^2\,\mathrm{g}^{-1}$, and B_λ and S_λ in MJy sr^{-1} and then Equation (6) is

$$S_\lambda = (2.0891 \times 10^{-4}) \kappa_\lambda \Sigma_d B_\lambda. \tag{7}$$

From Equation 6, it is clear that the values of κ_λ and Σ_d are completely degenerate. Without further information, FIR to submillimeter SED observations only constrain $\tau_\lambda = \kappa_\lambda \Sigma_d$. Breaking this degeneracy is possible in the one environment where we have measurements of the expected amount of dust independent from the measured FIR to submillimeter dust emission. This environment is the MW diffuse ISM where ultraviolet and optical gas-phase absorption measurements provide a strong constraint on the depletions in the ISM (e.g., Jenkins 2009). We use these measurements to calibrate κ_λ in Section 5 for the models introduced below. This calibration ensures that our models produce the right Σ_d in the one place where we know the correct value from independent measurements.

3.1. SMBB: Simple Emissivity Law Model

The SMBB predicts the surface brightness assuming a dust population with single dust temperature modified by a simple emissivity law (Hildebrand 1983). The adopted emissivity law is

$$\kappa_\lambda = \frac{\kappa^{\mathrm{S}}_{\mathrm{eff},160}}{160^{-\beta_{\mathrm{eff}}}} \lambda^{-\beta_{\mathrm{eff}}}. \tag{8}$$

The value of $\kappa^{\mathrm{S}}_{\mathrm{eff},160}$ is set by fitting of the diffuse MW SED (Section 5 and Table 2). The full set of fit parameters for the SMBB model are $\theta_{\mathrm{S}} = (\Sigma_d, T_{\mathrm{eff,d}}, \beta_{\mathrm{eff}})$. The values for the dust properties are effective values due to composition and temperature mixing along the line of sight and are not directly comparable to interstellar dust grain analogs studied in the laboratory (see Section 1).

3.2. BEMBB: Broken Emissivity Law Model

The BEMBB predicts the surface brightness assuming a dust population with a single dust temperature modified by a broken emissivity law. The adopted emissivity law is

$$\kappa_\lambda = \frac{\kappa^{\mathrm{BE}}_{\mathrm{eff},160}}{160^{-\beta_{\mathrm{eff},1}}} E(\lambda) \tag{9}$$

and

$$E(\lambda) = \begin{cases} \lambda^{-\beta_{\mathrm{eff},1}} & \lambda < \lambda_b \\ (\lambda_b^{\beta_{\mathrm{eff},2}-\beta_{\mathrm{eff},1}})\lambda^{-\beta_{\mathrm{eff},2}} & \lambda \geqslant \lambda_b \end{cases}, \tag{10}$$

where λ_b is the break wavelength and is limited to $\geqslant 175\,\mu$m. This emissivity law is similar in form to that used by Li & Draine (2001) for astronomical silicates. The value of $\kappa^{\mathrm{BE}}_{\mathrm{eff},160}$ is set by the fitting of the diffuse MW SED (Section 5 and Table 2).

As we are particularly interested in measuring the submillimeter excess, we define the submillimeter excess as the excess emission at a particular submillimeter wavelength above or below that expected for a SMBB model with $\beta_{\mathrm{eff}} = \beta_{\mathrm{eff},1}$. Given the BEMBB model definition, the submillimeter excess at $500\,\mu$m is

$$e_{500} = \left(\frac{\lambda_b}{500}\right)^{\beta_{\mathrm{eff},2}-\beta_{\mathrm{eff},1}} - 1. \tag{11}$$

Using e_{500} as one of the fit parameters (instead of $\beta_{\mathrm{eff},2}$), the fit parameters for the BEMBB model are $\theta_{\mathrm{BE}} = (\Sigma_d, T_{\mathrm{eff,d}}, \beta_{\mathrm{eff},1}, \lambda_b, e_{500})$. Note that the value of e_{500} can be negative and this would indicate a submillimeter deficit. The values for the dust properties are effective values due to composition and temperature mixing along the line of sight and are not directly comparable to interstellar dust grain analogs studied in the laboratory (see Section 1).

3.3. TTMBB: Two-temperature Model

The TTMBB predicts the surface brightness assuming two dust populations with distinctly different dust temperatures modified by a single, nonbroken emissivity law. The surface brightness is then

$$S_\lambda = \kappa_\lambda \left[\Sigma_{d1} B_\lambda(T_{\mathrm{eff},d1}) + \Sigma_{d2} B_\lambda(T_{\mathrm{eff},d2})\right], \tag{12}$$

where

$$\kappa_\lambda = \frac{\kappa^{\mathrm{TT}}_{\mathrm{eff},160}}{160^{-\beta_{\mathrm{eff}}}} \lambda^{-\beta_{\mathrm{eff}}}, \tag{13}$$

the subscripts $d1$ and $d2$ refer to the two dust components, and $T_{\mathrm{eff},d1} > T_{\mathrm{eff},d2}$. The value of $\kappa^{\mathrm{TT}}_{\mathrm{eff},160}$ is set by fitting of the diffuse MW SED (Section 5 and Table 2).

For this model, the submillimeter excess at $500\,\mu$m is

$$e_{500} = \frac{\Sigma_{d2} B_{500}(T_{\mathrm{eff},d2})}{\Sigma_{d1} B_{500}(T_{\mathrm{eff},d1})}. \tag{14}$$

Again, we use e_{500} as a fit parameter and the full set of fit parameters for the TTMBB model are $\theta_{\mathrm{TT}} = (\Sigma_{d1}, T_{\mathrm{eff},d1}, T_{\mathrm{eff},d2}, \beta_{\mathrm{eff}}, e_{500})$. Note that the value of e_{500} for the TTMBB model *cannot* be negative, unlike the case for the BEMBB model. The values for the dust properties are effective values due to composition and temperature mixing along the line of sight and are not directly comparable to interstellar dust grain analogs studied in the laboratory (see Section 1).

3.4. Restricted β_{eff} Models

It is often assumed in modified blackbody fitting that only β_{eff} values between one and two are valid. This is based on arguments that laboratory measurements of dust analogs only give β values between these limits. More precisely, laboratory measurements of carbonaceous and silicate dust analogs give β values between 0.8 and 2.5 for the *Herschel* wavelength range (e.g., Jager et al. 1998; Coupeaud et al. 2011). It is clear that luminosity weighted mixing of dust analogs with β values between 0.8 and 2.5 will always result in β_{eff} values in the same range. However, this is not necessarily the case for temperature mixing along the line of sight (Juvela & Ysard 2012). Combining the effects of composition and temperature mixing using full radiative transfer models, Ysard et al. (2012) give evidence that find that an β_{eff} (β_{color} in their terminology) between 0.8 and 2.5 is reasonable for a range of realistic cases. Thus, we include versions of the SMBB, BEMBB, and TTMBB models that have β_{eff} values restricted to be between 0.8 and 2.5. However, we caution that it is more statistically correct to include β_{eff} values outside this range as measurement noise can create SEDs that require nonphysical β_{eff} values to provide statistically robust fits.

3.5. Band Integration

Our models produce SEDs that are well sampled in wavelength, but our observations have a very coarse wavelength sampling as they are taken through filters with broad response functions. It is important to correctly model the effects of these broad response functions on the models to give accurate fits to the observations. For this paper, we start with the model predictions of the surface brightnesses at a wavelength resolution that well resolves the PACS and SPIRE bandpasses (Müller et al. 2011b; Griffin et al. 2013). Then, the band surface brightnesses were determined by integrating over their respective band response functions using

$$S_{\text{band}} = \frac{\int S_\nu R_E(\nu)\,d\nu}{\int (\nu_o/\nu)^{-1} R_E(\nu)\,d\nu}, \qquad (15)$$

where $R_E(\lambda)$ is the response function appropriate for extended sources given in fractional transmitted energy. The $\nu_o = c/\lambda_o$ values are given by $\lambda_o = 100$, 160, 250, 350, and 500 μm for the bands with the same names. Equation (15) mathematically models the data that is produced by the PACS and SPIRE instruments and data reduction pipelines. The integration is done in energy units (e.g., MJy sr^{-1}) as both instruments use bolometers that measure energy (not photons). The denominator of this equation normalizes $R_E(\lambda)$ and accounts for the PACS and SPIRE calibration convention where the calibration is given at specific wavelengths (λ_0) and for a $S(\nu) = \nu^{-1}$ reference spectrum.

4. FITTING TECHNIQUE

We computed the models on discrete grids with spacings fine enough to resolve the final one-dimensional (1D) likelihoods for each parameter. The grids were computed over a large range in each parameter to ensure that the likelihood function was well sampled. The ranges and spacings for both models are given in Table 1. We use a logarithmic spacing for Σ_d to provide a computationally efficient sampling of the full dynamic range of this parameter. The minimum and maximum ranges of the parameters were set iteratively, expanding the fit parameter

Table 1
Grid Parameters

Parameter	Range	Spacing
SMBB		
$\log(\Sigma_d)$ ($M_\odot$ pc^{-2})	-4 to 1	0.1
$T_{\text{eff,d}}$ (K)	5 to 75	1
β_{eff}	-1 to 4	0.25
BEMBB		
$\log(\Sigma_d)$ ($M_\odot$ pc^{-2})	-4 to 1	0.1
$T_{\text{eff,d}}$ (K)	5 to 75	1
$\beta_{\text{eff,1}}$	-1 to 4	0.25
λ_b (μm)	175 to 375	25
e_{500}	-1 to 2	0.25
TTMBB		
$\log(\Sigma_{d1})$ ($M_\odot$ pc^{-2})	-4 to 1	0.1
$T_{\text{eff,d1}}$ (K)	5 to 75	2
$T_{\text{eff,d1}}$ (K)	4 to 75	2
β_{eff}	-1 to 4	0.25
e_{500}	0 to 2	0.25

ranges until the 1D likelihood function for the vast majority of the pixels in the galaxies were well sampled.

We fit each pixel that was detected at 3σ above the background in all five bands. The probability that a particular model fits the data was computed assuming a multi-variate Normal/Gaussian distribution (Gut 2009) using

$$P(S^{\text{obs}} \mid \theta) = \frac{1}{Q} \exp\left(-\frac{1}{2}\chi^2(\theta)\right), \qquad (16)$$

where

$$Q^2 = (2\pi)^n \det|\mathbb{C}| \qquad (17)$$

and

$$\chi^2(\theta) = [S^{\text{obs}} - S^{\text{mod}}(\theta)]^T \mathbb{C}^{-1}[(S^{\text{obs}} - S^{\text{mod}}(\theta)]. \qquad (18)$$

S^{obs} is the observed SED for a single pixel in the $n = 5$ bands, S^{mod} is the SED for a particular model and parameter set, θ, and $\mathbb{C}$ is the covariance matrix. The ^{T} notation denotes the transpose of the vector. The covariance matrix is often given as the Σ symbol, but we have chosen to use $\mathbb{C}$ to avoid confusion with the dust surface density or standard summation symbol.

The explicit use of a covariance matrix in the fitting allows us to directly account for correlations between bands in the data. This is a different approach than has been recently taken by other authors. One technique for investigating the effects of correlated noise on model fit parameters is to perform many Monte Carlo trials of the observations where they are perturbed by the random and correlated noise and fit with the model (e.g., Galliano et al. 2011). A second technique is to include parameters in a hierarchical Bayesian model for the correlations in the absolute flux calibration between bands and then marginalize (integrate) over them to determine their final fit probabilities (e.g., Kelly et al. 2012). While not often done, it is critical to account for the correlated noise in observations as neglecting such noise terms can significantly bias the resulting fit parameters (Veneziani et al. 2013). By including the covariance directly into the likelihood function we do not need to perform many Monte Carlo trials for every pixel or use a hierarchical Bayesian model to account for this noise term. In other words, we can include the correlations directly in the individual fits efficiently without having to appeal to the ensemble behavior.

4.1. LMC and SMC Covariance Matrices

For this work, the covariance matrix is defined as

$$\mathbb{C} = \mathbb{C}_{\mathrm{cal}} + \mathbb{C}_{\mathrm{bkg}}, \tag{19}$$

where $\mathbb{C}_{\mathrm{cal}}$ is the absolute surface brightness covariance matrix and $\mathbb{C}_{\mathrm{bkg}}$ is the background covariance matrix. The units of these covariance matrices are $(\mathrm{MJy\ sr}^{-1})^2$.

The $\mathbb{C}_{\mathrm{cal}}$ is given by the details of the PACS and SPIRE absolute flux calibrations. The SPIRE instrument has been calibrated using a model of Neptune with an absolute uncertainty correlated between bands for point sources of 4% and a repeatability that is uncorrelated between bands of 1.5% (Griffin et al. 2013; Bendo et al. 2013). For extended sources, it is recommended to add an additional 4% to account for the correlated uncertainty in the total beam area resulting in an 8% correlated uncertainty between bands (Herschel Space Observatory 2011). The PACS instrument has been calibrated using models of stars and asteroids with an absolute uncertainty correlated between bands for point sources of 5% and a repeatability uncorrelated between bands of 2% (Müller et al. 2011a; Balog et al. 2013). Similar to SPIRE, for extended sources we add an additional 5% correlated uncertainty to account for uncertainties in the total beam area resulting in a 10% correlated uncertainty between bands. Finally, we assume the PACS and SPIRE calibrations are independent given that PACS is calibrated using stars and SPIRE using Neptune. Given this information, the elements of $\mathbb{C}_{\mathrm{cal}}$ are

$$(\mathbb{C}_{\mathrm{cal}})_{ij} = S_i^{\mathrm{mod}}(\theta) S_j^{\mathrm{mod}}(\theta) \left[(\mathbf{A}_{\mathrm{cor}})_{ij} + (\mathbf{A}_{\mathrm{uncor}})_{ij} \right], \tag{20}$$

where

$$\mathbf{A}_{\mathrm{cor}} = \begin{bmatrix} 0.1^2 & 0.1^2 & 0 & 0 & 0 \\ 0.1^2 & 0.1^2 & 0 & 0 & 0 \\ 0 & 0 & 0.08^2 & 0.08^2 & 0.08^2 \\ 0 & 0 & 0.08^2 & 0.08^2 & 0.08^2 \\ 0 & 0 & 0.08^2 & 0.08^2 & 0.08^2 \end{bmatrix} \tag{21}$$

and

$$\mathbf{A}_{\mathrm{uncor}} = \begin{bmatrix} 0.02^2 & 0 & 0 & 0 & 0 \\ 0 & 0.02^2 & 0 & 0 & 0 \\ 0 & 0 & 0.015^2 & 0 & 0 \\ 0 & 0 & 0 & 0.015^2 & 0 \\ 0 & 0 & 0 & 0 & 0.015^2 \end{bmatrix}. \tag{22}$$

The background covariance matrix, $\mathbb{C}_{\mathrm{bkg}}$ is calculated empirically from a large set of pixels visually identified as lying outside of the emitting region of each galaxy. The background pixels are in the full images and were processed as described in Section 2. The terms of the covariance matrix are calculated using

$$\sigma_{ij}^2 = \frac{\sum_k^N (S_i^k - \langle S_i \rangle)(S_j^k - \langle S_j \rangle)}{N - 1}, \tag{23}$$

where N is the number of background pixels, S_i^k / S_j^k is the ith/jth band of the kth pixel, and $\langle S_i \rangle / \langle S_j \rangle$ is the average background

in the ith/jth band. For the LMC, $N = 52113$ and

$$\mathbb{C}_{\mathrm{bkg}}(\mathrm{LMC}) = \begin{bmatrix} 4.23 & 0.78 & 0.65 & 0.33 & 0.14 \\ 0.78 & 2.37 & 0.85 & 0.43 & 0.18 \\ 0.65 & 0.85 & 0.91 & 0.47 & 0.20 \\ 0.33 & 0.43 & 0.47 & 0.25 & 0.11 \\ 0.14 & 0.18 & 0.20 & 0.11 & 0.057 \end{bmatrix} \tag{24}$$

and for the SMC, $N = 4012$ and

$$\mathbb{C}_{\mathrm{bkg}}(\mathrm{SMC}) = \begin{bmatrix} 2.64 & 0.56 & 0.30 & 0.14 & 0.064 \\ 0.56 & 1.18 & 0.46 & 0.23 & 0.094 \\ 0.30 & 0.46 & 0.36 & 0.20 & 0.089 \\ 0.14 & 0.23 & 0.20 & 0.12 & 0.054 \\ 0.064 & 0.094 & 0.089 & 0.054 & 0.030 \end{bmatrix}. \tag{25}$$

These empirical covariance matrices illustrate that background is highly correlated with the correlation increasing in strength toward longer wavelengths. This is illustrated by the correlation matrix (terms are $\mathbb{C}_{ij}/[\sigma_i \sigma_j]$) for the SMC:

$$\mathrm{corr}_{\mathrm{bkg}}(\mathrm{SMC}) = \begin{bmatrix} 1.00 & 0.32 & 0.31 & 0.25 & 0.23 \\ 0.31 & 1.00 & 0.70 & 0.61 & 0.49 \\ 0.30 & 0.70 & 1.00 & 0.94 & 0.85 \\ 0.25 & 0.61 & 0.94 & 1.00 & 0.91 \\ 0.23 & 0.49 & 0.85 & 0.91 & 1.00 \end{bmatrix}. \tag{26}$$

The LMC correlation matrix is very similar and thus is not shown. The positive and nonzero correlation terms are signatures that the correlated noise in the background is due to real astronomical signals. In this case, it is traceable to the residual foreground MW cirrus emission and the integrated emission from background galaxies. The higher covariance values for the LMC is a reflection of the increased difficulty of background subtraction for this galaxy.

4.2. Example Fitting Results

The fitting technique we use fully computes the nD likelihood function that a particular model fits the SED of a pixel where n is the number of fit parameters. One way to visualize the results is to create 1D likelihood functions for each fit parameter by marginalizing (integrating) over all the other parameters. This is shown in Figure 1 for the BEMBB model for a single pixel in the SMC for three different assumptions; assuming uncorrelated uncertainties, including the full covariance, and including the full covariance while restricting $\beta_{\mathrm{eff},1}$ to vary between 0.8 and 2.5. The results for pixels in the LMC are similar. With the same overall uncertainties, we obtain a much narrower function with a stronger likelihood by including the known covariance between the bands (Section 4.1) than by assuming that there is no correlation between bands. In this case, including the known covariance between bands results in better constraints on the fit parameters as the allowed model space is reduced. The impact of a limited $\beta_{\mathrm{eff},1}$ range is shown in this figure where, not surprisingly, it makes for a narrower 1D likelihood function than allowing $\beta_{\mathrm{eff},1}$ to vary in order to fully sample the $\beta_{\mathrm{eff},1}$ 1D likelihood function. Note that this limitation simply crops the $\beta_{\mathrm{eff},1}$ 1D likelihood function, but changes the shape of the other 1D likelihood functions significantly.
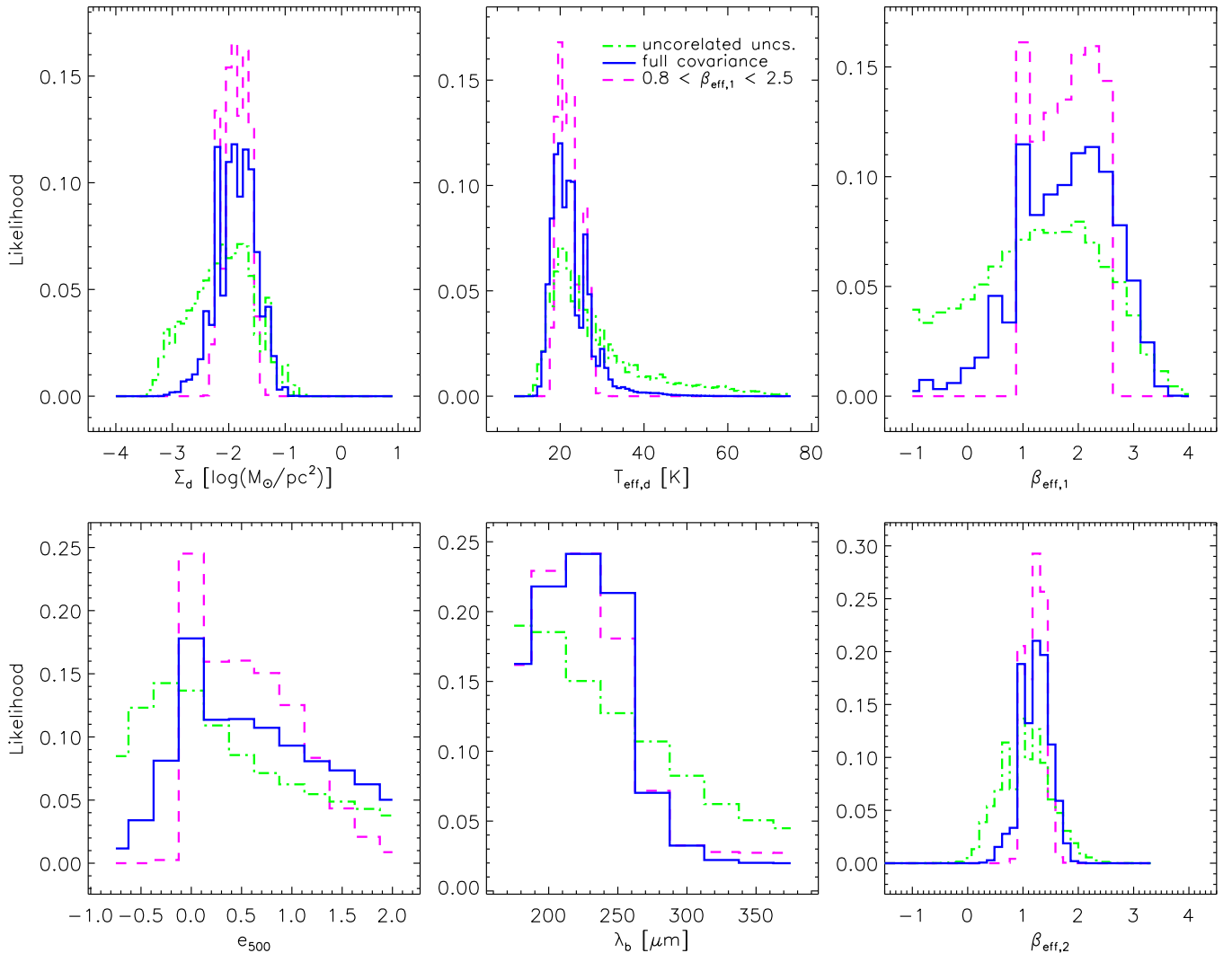
Figure 1. 1D likelihood functions for a single pixel in the SMC using the BEMBB model are plotted for fitting while assuming uncorrelated uncertainties, including the full covariance, and including the full covariance while restricting the allowed $\beta_{eff,1}$ values to be between 0.8 and 2.5. Note that $\beta_{eff,2}$ is completely determined by the value of $\beta_{eff,1}$ and e_{500}, and we present the $\beta_{eff,2}$ 1D likelihood function for completeness.

(A color version of this figure is available in the online journal.)

4.3. Sensitivity Tests

The goal of the sensitivity tests is to determine if there are systematic shifts in recovered parameters and if the uncertainty on the recovered parameters matches that measured from the widths of the 1D likelihood functions. We simulated observations by picking a model SED and adding noise using the Cholesky factorization of the covariance matrix appropriate as if the model was observed like the SMC was observed in HERITAGE. The results using the LMC noise model are very similar. We repeated the simulation for each model SED 20 times to provide a good sampling of the recovered fit parameter uncertainties and systematic offset from the input fit parameters.

As we are testing the ability of this fitting technique to recover parameters by fitting simulated observations, this requires a way to measure the recovery of the input model parameters. The main output of the fitting is the nD likelihood function, but it is often useful to distill these results to the "best-fit" or summary values. We use three different ways to define the "best-fit" values. The first is the most traditional definition of the "best fit" and corresponds to the maximum likelihood ("max"). This

is also called the "traditional χ^2" method in some papers (e.g., Kelly et al. 2012; Juvela et al. 2013). The "max" value is most useful when plotting the best-fitting model with observations or investigating the fitting residuals. The second is the expectation value ("exp") which is the likelihood weighted average of the parameter and is a reflection of the full likelihood function. This "exp" value reflects the best "average" value as it reflects the full likelihood function (not just the peak like the "max" value). We find the "exp" particularly useful for making images of the fit parameters. The third way to reflect the best fit is take a realization of the full nD likelihood function itself ("realize"). This involves randomly sampling the likelihood function and reflects the full likelihood function's shape in a statistical sense. The "realize" method is most useful when studying the ensemble behavior of the fit parameters for many pixels.

The results for runs with 2000 randomly picked BEMBB models are shown in Figure 2. All three different methods of determining the "best-fit" parameters give similar results with similar trends with each parameter. The "exp" gives the lowest systematic error in the recovery, but the "max" gives the lowest scatter. The "realize" method provides a nominally
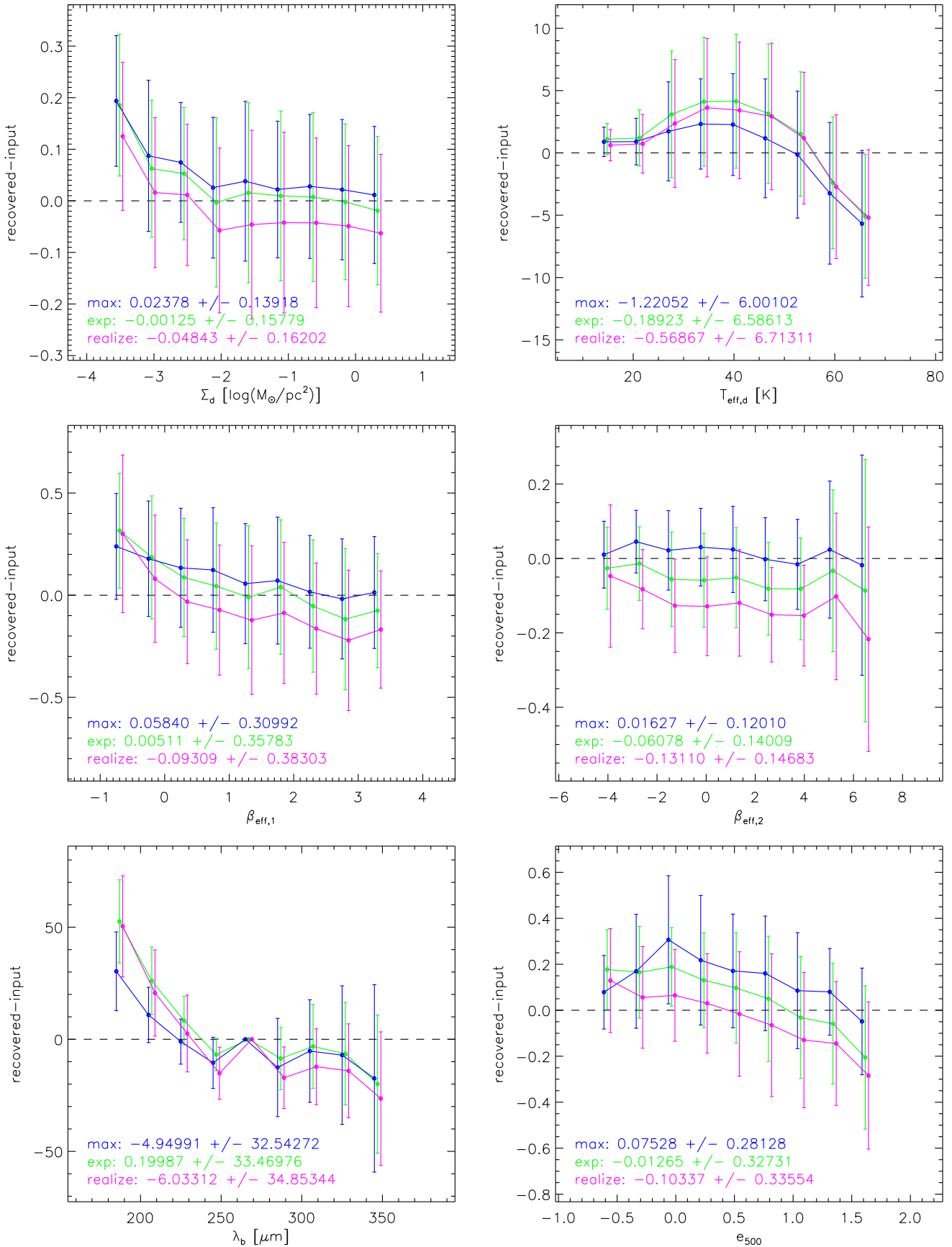
Figure 2. Results for sensitivity tests of the BEMBB model for 2000 models randomly selected from the full model grid are shown. The results are plotted as averages and standard deviations of the recovered minus input parameters in 10 bins over the parameter range. The three different methods of determining the accuracy of the recovered parameters are "max" = maximum likelihood, "exp" = expectation value, and "realize" = one realization based on the 1D likelihood functions for each parameter.

(A color version of this figure is available in the online journal.)

worse recovery than both the other methods, but is a fuller picture of true sensitivity of the fitting. Overall, which "best-fit" method used depends on the particular question being asked. We illustrate this later in this paper and in the companion paper on the gas-to-dust ratio (Roman-Duval et al. 2014).

Of particular interest for this paper is the fact that the recovery of the submillimeter excess, e_{500}, is good to around 10%, on average, for the "realize" method and around 1% for the "exp" method. For the companion paper (Roman-Duval et al. 2014), the fit parameter of main interest is Σ_d and the recovery is good, on average and in $\log(\Sigma_d)$ units, to 0.05 for the "realize" method and 0.001 for the "exp" method. This excellent recovery of $\log(\Sigma_d)$ holds even in the presence of significant scatter in $T_{\mathrm{eff,d}}$ and may be due to other parameters in the fitting varying to compensate. Note that, for the "exp" method, we computed the expectation value of $\log(\Sigma_d)$ because we found that the sensitivity tests showed significantly less systematic bias than if we computed the expectation value of Σ_d. We confirmed that the widths of the 1D likelihood functions match the noise in the recovery of the input model parameters.

4.4. Number of Parameters and Data Points

The number of parameters in our models are three, five, and five for the SMBB, BEMBB, and TTMBB models, respectively. In this paper, these models are fit to FIR-submillimeter SEDs that are composed of five data points. At first glance, this violates the rule that fitting requires at least one data point more than the number of fitting parameters to provide a unique solution. This is correct, if the fitting is done with a model that can fit any distribution of data points. This is clearly not the case for our models since they are all constrained to have a spectral shape of one or two modified blackbodies. In other words, they cannot fit arbitrary spectral shapes, but are constrained by our knowledge of the physics of dust grain emission. Effectively, we are using more than just five data points in our fits because we combine the data points with a larger body of observations that informs our understanding of dust physics and, therefore, the appropriate models to use. Finally, our use of full likelihood functions explicitly accounts for the impact of the number of parameters on how well we can determine each fit parameter. Using full likelihood functions has the additional benefit of measuring how well each parameter is constrained by the data explicitly. Some parameters are better constrained than others as shown in Figure 1. For example, Σ_d and $T_{\mathrm{eff,d}}$ are better constrained as the overall level and spectral shape are well constrained by the observations, but the detailed spectral shape is less well constrained and this strongly impacts $\beta_{\mathrm{eff,1}}$, λ_b, and e_{500}.

5. MODEL CALIBRATION

It is important to calibrate dust models to reproduce observations where there are independent measurements of the same quantities using the same fitting technique. This is regularly done when setting up full dust grain models (e.g., Li & Draine 2001; Zubko et al. 2004; Compiègne et al. 2011). One key calibration source is the FIR–submillimeter SED of the MW diffuse ISM. This is a unique environment because it is the one place where the amount of dust has been measured using ultraviolet and optical gas-phase absorption lines and knowledge of the total amount of atoms expected in the ISM (e.g., Jenkins 2009). Thus, fitting the FIR-submillimeter MW diffuse SED results in

a calibration of the dust emissivity κ_λ as the degeneracy between this quantity and Σ_d is removed.

In full dust grain models, the calibration of κ_λ is usually set such that the luminosity weighted average response of the different dust grain components reproduces the MW diffuse SED when the dust is illuminated by the average MW radiation field. In a similar manner, the $\kappa_{\mathrm{eff,160}}$ for the models used in this paper is set such that fitting the MW diffuse SED produces the observed gas-to-dust ratio. By determining $\kappa_{\mathrm{eff,160}}$ using the measurements of the diffuse MW emission for each of our models, we ensure that our models derive the correct dust surface density in the one physical environment where we have independent constraints on the dust mass. It is critical to note that this calibration does not impose a gas-to-dust ratio calibration on our model, just a calibration that we derive the correct mass of dust in the MW diffuse ISM.

This calibration does mean that we are assuming that the dust properties in the Magellanic clouds are the same as those in the diffuse MW. This assumption is reasonable given the evidence from ultraviolet extinction measurements in all three galaxies. The SMC does show UV extinction curves that are most different from the average in the MW, but it also has curves that are very similar to the MW average (Gordon & Clayton 1998; Maíz Apellániz & Rubio 2012). The LMC shows extinction curves that are similar or equivalent to the MW average (Misselt et al. 1999; Gordon et al. 2003). While many of the MW lines of sight show extinction curves similar to the MW average by definition (Valencic et al. 2004), there is one line of sight that shows a UV extinction curve that is indistinguishable from the most different SMC extinction curves (Valencic et al. 2003). It is not clear if the globally average UV dust extinction is different between the three galaxies, mainly due to small samples sizes of such measurements in the Magellanic clouds (Gordon et al. 2003). One piece of evidence that far-IR emissivity of dust grains is similar between the MW and SMC is the similarity of their $\kappa_{\mathrm{eff,160}}$ values as derived using dust grain model fitting (see Section 5.3). While it is reasonable to assume the dust is similar in all three galaxies, it is an assumption and the dust surface densities will vary inversely in direct proportion to any changes in the adopted $\kappa_{\mathrm{eff,160}}$ calibration.

Evidence for MW dust that is different from that in the LMC was found in work by Meixner et al. (2010) and Galliano et al. (2011) using the HERITAGE test observations of a strip in the LMC. These works used two models of dust, one composed of silicates, graphite, and PAH grains that describes average MW dust ("standard") and a second with amorphous carbon instead of graphite ("AC"). The analysis found that the gas-to-dust ratio for the "standard" model was lower than a reasonable ratio for LMC metallicity, while the "AC" model produced a reasonable ratio. We discuss the issue of gas-to-dust ratios for the LMC and SMC using the fitting results for the models used in this paper and calibrated using the MW diffuse SED in Section 6.3. In addition, we have estimated the systematic error on $\kappa_{\mathrm{eff,160}}$ due to the assumption that the dust is like that in the MW in Section 5.3.

Direct measurements of ISM depletions in the Magellanic clouds would allow us to directly calibrate our models in these galaxies. This would remove the assumption that the dust grain compositions in the Magellanic clouds are the same as those in the MW. Currently, there exists only a limited number of sightlines and atoms with measured depletions in the Magellanic clouds (Roth & Blades 1997; Welty et al. 1997, 2001; Sofia et al. 2006; Peimbert & Peimbert 2010; Welty & Crowther 2010). Extending these studies in terms of atomic species and

Table 2
MW Diffuse Fit Results

Model	$\kappa_{\mathrm{eff},160}$[a] (cm^2 g^{-1})	Other Parameters	Expectation Values
SMBB	$9.6 \pm 0.4 \pm 2.5$	$(T_{\mathrm{eff,d}}, \beta_{\mathrm{eff}})$	$(17.2 \pm 0.4\ \mathrm{K}, 1.96 \pm 0.10)$
BEMBB	$11.6 \pm 1.5 \pm 2.5$	$(T_{\mathrm{eff,d}}, \beta_{\mathrm{eff},1}, \lambda_b, e_{500})$	$(16.8 \pm 0.6\ \mathrm{K}, 2.27 \pm 0.15, 294 \pm 29\ \mu\mathrm{m}, 0.48 \pm 0.11)$
TTMBB	$517 \pm 214 \pm 2.5$	$(T_{\mathrm{eff,d1}}, T_{\mathrm{eff,d2}}, \beta_{\mathrm{eff}}, e_{500})$	$(15.0 \pm 0.7\ \mathrm{K}, 6.0 \pm 0.8\ \mathrm{K}, 2.9 \pm 0.1, 0.91 \pm 0.25)$
TTMBB	$9.6 \pm 0.4 \pm 2.5$	Adopted	

Note. [a] The results are given as value $\pm$ fitting uncertainty $\pm$ systematic uncertainty
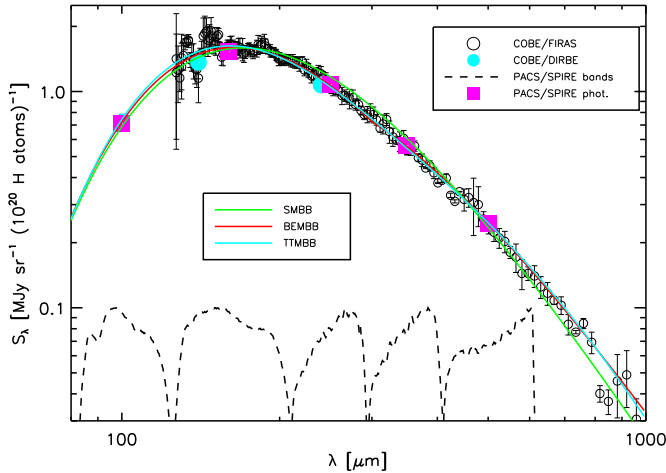
Figure 3. Observed MW diffuse SED from COBE, FIRAS, and DIRBE is plotted along with the best fits for the models used in this paper. The best fit is defined using the "max" method discussed in Section 4.3. The "PACS/SPIRE phot." points (purple squares) are those used to constrain the fits of the models and were derived from the COBE, FIRAS, and DIRBE measurements.

(A color version of this figure is available in the online journal.)

galactic environments should be a priority for the astronomical community, since they are critical for interpreting the wealth of FIR to submillimeter ISM observations obtained by recent space missions.

5.1. Milky Way Diffuse SED

For the diffuse MW emission, we use the Compiègne et al. (2011) measurement where emission was measured by correlating the IR versus H I emission maps in atomic gas dominated regions of the MW. The IR measurements we use are mainly the COBE/FIRAS spectrophotometry from 127 to 1200 μm supplemented by the DIRBE 100 μm photometry. Because we want to calibrate our models using the same bands as used for the HERITAGE observations, we integrated this diffuse MW SED using the method described in 3.5 for all the bands except the PACS 100 μm band. For this band, we adopted the DIRBE 100 μm measurement since the bandpasses are similar. The resulting MW diffuse SEDs are 0.71, 1.53, 1.08, 0.56, and 0.25 MJy sr^{-1} (10^{20} H atom)$^{-1}$ for the 100, 160, 250, 350, and 500 μm and are plotted in Figure 3. These values differ from those given for the same bands by Compiègne et al. (2011) mostly because we have not included the 0.77 correction for ionized gas. In addition, there are minor differences in the response curves used. We do not include the 0.77 correction for ionized gas because the depletion measurements do not include any ionized gas correction. For the uncertainties, we have assumed 5% correlated and 2.5% uncorrelated terms (see Section 3.5) given the high quality of the COBE, FIRAS, and DIRBE calibrations.

5.2. Milky Way Diffuse Gas-to-dust Ratio

Because the MW diffuse SED is measured as a correlation between dust and gas emission, the constraint we need is the MW diffuse gas-to-dust ratio. We use the work of Jenkins (2009) to determine the appropriate gas-to-dust ratio since this work provides an excellent compilation and summary of MW depletions. The observed H columns of our adopted FIR-submillimeter MW diffuse SED are $\log[N(H)] < 20.7$. The average depletion of all the sightlines with these column densities tabulated by Jenkins (2009) is $F_* = 0.36$. F_* is the depletion factor and measures the overall depletions in a sightline. Using the depletion fits of Jenkins (2009) with $F_* = 0.36$, the diffuse MW gas-to-dust ratio is computed to be 150.

5.3. Calibrating $\kappa_{eff,160}$

We calibrate the value of $\kappa_{\mathrm{eff},160}$ in each of our models so that they reproduce the MW diffuse observed gas-to-dust ratio of 150. For our work, we have chosen 160 μm to set our normalization of $\kappa_{\mathrm{eff},\lambda}$ because shorter wavelengths have a weaker dependence on temperature based on laboratory investigations of dust analogs (Coupeaud et al. 2011). The $\kappa_{\mathrm{eff},160}$ values required for each model based on the "exp" method of determining the best fits (see Section 4.3) are given in Table 2. The second uncertainty on $\kappa_{\mathrm{eff},160}$ is an estimate of the systematic uncertainty (see next paragraph). The fit parameters for each model are also given in this table, along with 1σ uncertainties. The larger relative uncertainties on $\kappa_{\mathrm{eff},160}$ for the BEMBB model as compared to the SMBB can be directly traced to the larger number of BEMBB fit parameters. The "max" best-fit models are plotted in Figure 3.

The $\kappa_{\mathrm{eff},160}$ values for the SMBB and BEMBB models agree favorably with other determinations while the value for the TTMBB model does not. For example, if "astronomical" silicate grains with $a = 0.1\mu$m and $\rho = 3$ g cm^{-3} are used, then $\kappa_{\mathrm{eff},160} = 13.75$ cm^2 g^{-1}. Such grain properties are often assumed for simple modified blackbody fits because this is the average size for a Mathis et al. (1977) grain size distribution (Hildebrand 1983). The widely used Weingartner & Draine (2001) full dust grain model for $R(V) = 3.1$ has a $\kappa_{\mathrm{eff},160} = 9.97$ cm^2 g^{-1}. The updated version of this model has a $\kappa_{\mathrm{eff},160} = 12.5$ cm^2 g^{-1} (Draine & Li 2007; Draine et al. 2014). The $\kappa_{\mathrm{eff},160}$ values for the Zubko et al. (2004) models that include graphite and amorphous carbon range from 10.75 to 15.0 cm^2 g^{-1}. Finally, the Weingartner & Draine (2001) model for the SMC Bar extinction curve with no 2175 Å extinction feature has $\kappa_{\mathrm{eff},160} = 13.1$ cm^2 g^{-1}. Using the range of these model $\kappa_{\mathrm{eff},160}$ values, we estimate that there is a ± 2.5 cm^2 g^{-1} additional uncertainty on $\kappa_{\mathrm{eff},160}$ due to systematic uncertainties in our knowledge of dust grains.

The TTMBB model with $\kappa_{eff,160} = 517 \pm 214$ cm^2 g^{-1} requires a dust grain that is very efficient at emission, yet this level of efficiency is much higher than any astronomically reasonable dust grain. A much simpler explanation is that the dust in the MW diffuse ISM is not well modeled by a TTMBB model that includes a very cold ($T_{eff,d} \sim 6$ K) dust grain population. This is the same conclusion given by the Reach et al. (1995) analysis of the FIRAS data. There still may be regions in the ISM of the MW or other galaxies that are well described by the TTMBB model. To allow for such regions, we adopt the $\kappa_{eff,160}$ of the SMBB model as the value for the TTMBB model.

The variations in the $\kappa_{eff,160}$ values in the literature and between the different models used in this paper clearly indicate that $\kappa_{eff,160}$ is sensitive to the model assumptions. Thus, it is important to calibrate each model explicitly with the diffuse MW SED and a depletion measured gas-to-dust ratio. This is a standard calibration method for dust grain models (Draine & Li 2007; Compiègne et al. 2011) and we advocate that such calibrations be done for all dust emission models (Bianchi 2013). Such model calibrations will allow for meaningful comparisons between the results from different models.

6. RESULTS

6.1. Fitting Residuals

One obvious question is: which model, SMBB, BEMBB, or TTMBB, fits the observations best? The answer to this question will give an indication of the origin of the submillimeter excess. The most straightforward method to test how well a model fits the data is to examine the residuals of the data to the fits. The χ^2 value computed using Equation (18) gives such a quantitative measure of the residuals. For the SMC, the pixel averaged χ^2 value is 3.47 for the SMBB model, 0.88 for the BEMBB model, and 1.83 for the TTMBB. The models with $0.8 < \beta_{eff} < 2.5$ have higher average χ^2 values than the unconstrained versions. For example, the β_{eff} constrained version of the BEMBB model for the SMC has an average χ^2 value of 1.32. The LMC average χ^2 values behave similarly.

More evidence that the BEMBB fits the data best (out of the three models) can be found by examining the behavior of the fit residuals versus surface brightness. Figure 4 shows the fit residuals for the SPIRE 250 μm band for all three models used in this paper for both Magellanic clouds. The trends for other bands are similar, especially in the relative behavior of the fit residuals between the models. This figure clearly shows that the simplest model (SMBB) has residuals larger than expected given the known uncertainties. This holds for β_{eff} unconstrained and constrained to be between 0.8 and 2.5. In addition, the residuals for the SMC have a systematic trend with more negative residuals at intermediate surface brightnesses. Such a trend is not consistent with the uncertainties in the absolute flux calibration or the background subtraction. Of all models, the BEMBB model without any constraint on β_{eff} fits the data best. Overall, the BEMBB model shows the smallest residuals with no obvious trend with surface brightness unlike the other models. The BEMBB model consistently shows smaller residuals in all the bands, not just the SPIRE 250 μm band. The other models have higher overall residuals and show systematic offsets and/or trends with surface brightness. The BEMBB and TTMBB models have the same number of fit parameters, yet the behavior of their residuals are different. This illustrates that it is not

Table 3
Integrated Dust Masses and Gas-to-dust Ratios Integrated over $>3\sigma$ Pixels

Model	M_d ($M_\odot$)	Gas/Dust[a]
	LMC	
SMBB	$(8.1 \pm 0.07 \pm 2.1) \times 10^5$	340 ± 90
BEMBB[b]	$(6.7 \pm 0.03 \pm 1.7) \times 10^5$	400 ± 100
TTMBB	$(1.2 \pm 0.01 \pm 0.3) \times 10^7$	22 ± 6
Expected: scaling MW gas-to-dust ratios		200–500
Expected: MW depletions and LMC abundances		150–360
Expected: all metals in dust		$\geqslant 105$
	SMC	
SMBB	$(8.1 \pm 0.1 \pm 2.1) \times 10^4$	1440 ± 380
BEMBB[b]	$(6.7 \pm 0.1 \pm 1.7) \times 10^4$	1740 ± 440
TTMBB	$(5.1 \pm 0.3 \pm 1.3) \times 10^5$	230 ± 60
Expected: scaling MW gas-to-dust ratios		500–1250
Expected: MW depletions and SMC abundances		540–1300
Expected: all metals in dust		$\geqslant 300$

Notes.
[a] The integrated gas masses in $M_\odot$ for the same areas and with the same background removal in the LMC/SMC are $2.5 \times 10^8/1.0 \times 10^8$ for H I and $2.1 \times 10^7/1.6 \times 10^7$ for H$_2$ (Leroy et al. 2007a; Hughes et al. 2010).
[b] Model favored from the analysis in this paper (see Section 6.1 and Section 6.3).

only the number of fit parameters that is critical for the fitting accuracy, but also the allowed spectral shapes.

Overall, the BEMBB spectral shapes fit the data better than the TTMBB and SMBB spectral shapes. This is evidence that the submillimeter excess is more likely to be due to emissivity variations than a second population of cold dust.

6.2. Total Dust Masses

The total dust masses are of interest for studies of the lifecycle of dust in the LMC and SMC (Boyer et al. 2012; Matsuura et al. 2013; Zhukovska & Henning 2013). In addition, they can be used along with the total gas masses as a way to tell if a model produces realistic amounts of dust (see Section 6.3).

We give the dust masses for the different models in Table 3 integrated over the $>3\sigma$ pixels. The restricted β_{eff} version of the models produces results that are very similar and are not given in the table. The dust mass values are given as total $\pm$ statistical uncertainty $\pm$ uncertainty due to the $\kappa_{eff,160}$ uncertainty. To convert from dust surface density to dust mass, we use distances of 60 kpc (Hilditch et al. 2005) and 50 kpc (Walker 2012) for the SMC and LMC, respectively. The total dust masses are computed from the "realize" method to produce dust surface density maps that provide a full accounting of the likelihood functions for all pixels. Ten different maps were made for each galaxy using the "realize" method that samples the likelihood function once for each pixel. This provides a robust measurement of the impact of the fitting noise of each pixel in the integrated dust mass measurement. The average and statistical uncertainty of the integrated dust mass were computed from the 10 maps. The large number of pixels in each galaxy result in the total dust mass changing only slightly between different realizations and this is the origin of the small statistical uncertainty. These dust masses are integrated only over the areas that were detected at 3σ above the background in all five *Herschel* bands measured by HERITAGE. Pixels $>3\sigma$ contribute 0.79, 0.73, 0.62, 0.61, and 0.61 of the SMC global fluxes of 15.7, 20.8, 14.5, 8.3, and 3.9 kJy for the PACS100, PACS160, SPIRE250, SPIRE350, and SPIRE500, respectively.
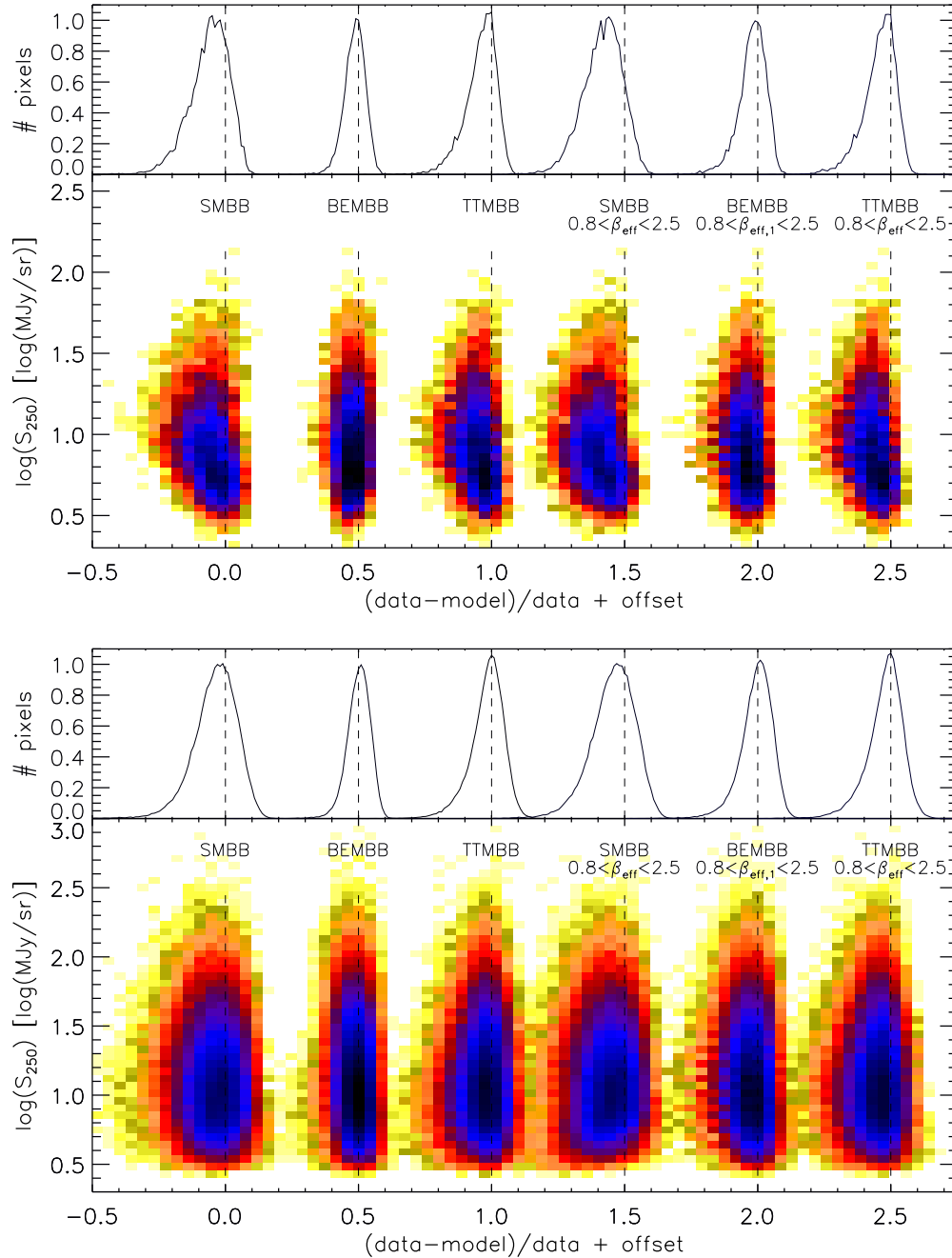
Figure 4. Fractional residuals for the SMC (top) and LMC (bottom) of the fits for the SPIRE 250 μm band are shown for all the models. Each model has been plotted shifted by multiples of 0.5 on the x axis. The false color gives the log density of points, and each point represents the residual for the "max" estimator for a single pixel. The "max" estimator was used to give each model the best chance to have the lowest residuals. The plots at other wavelengths show similar behaviors with the BEMBB model having the lowest residuals.

(A color version of this figure is available in the online journal.)

For the LMC, these fractions are 0.91, 0.89, 0.87, 0.87, and 0.87 for global fluxes of 223, 259, 142, 73, and 31 kJy for the same bands. The global fluxes quoted here differ from those given by Meixner et al. (2013) due to our subtraction of MW cirrus foreground and the additional background subtraction step.

The quantitative impact of correctly including the correlated noise in the measurements can be illustrated by noting that assuming the noise is uncorrelated between bands results in the BEMBB model giving fits with a total SMC dust mass that is ∼50% higher than the total dust mass given in Table 3.

The importance of accounting for the full likelihood function is equally important: the total SMC dust mass for the BEMBB model is ∼50% higher using the "max" values and ∼30% lower using the "exp" values of $\log(\Sigma_d)$ when compared to the "realize" value given in Table 3. The "realize" values are the correct values for determining the total dust mass values as they statistically reflect each pixel's full likelihood function, asymmetries and all, in the sum of the individual pixel masses. The "max" and "exp" values only reflect a limited portion of the likelihood function and this systematically biases the results.
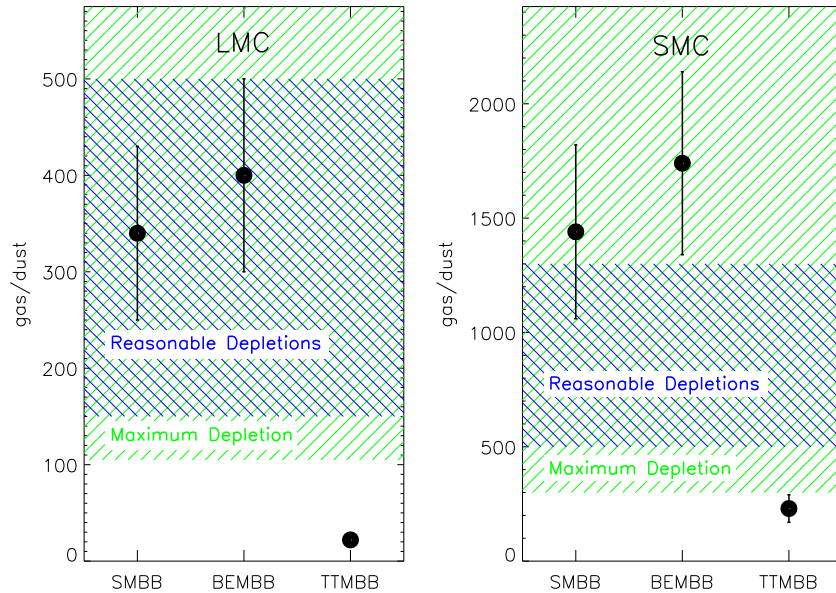
Figure 5. Gas-to-dust ratios (GDRs) are plotted as black circles for each of the three models and for both galaxies. The "reasonable" GDR range expected from scaling the MW diffuse to dense GDRs is given as a blue hatched region. The GDR range allowed by assuming the "maximum" depletions is given as a green hatched region (e.g., a lower limit on the GDR).

(A color version of this figure is available in the online journal.)

This is additional evidence that the likelihood functions for Σ_d are not well behaved Gaussians centered on the "max" value (see Figure 1).

Our total dust masses are only lower limits because we do not include the dust responsible for the emission with surface brightnesses below 3σ in any band. We can estimate the dust mass due to these $<3\sigma$ regions by modeling the integrated flux of these regions for each galaxy. Basically, we fit the SED that is the difference from the global fluxes quoted above and the integrated fluxes from $<3\sigma$ pixels. The resulting integrated dust masses for the BEMBB model and the $<3\sigma$ pixels are $(5.9 \pm 3.6) \times 10^4$ and $(1.6 \pm 1.3) \times 10^4$ $M_\odot$ for the LMC and SMC, respectively. The uncertainties are quite large due to the low surface brightnesses and strong mixing of environments in these integrated SEDs. Combining the $<3\sigma$ pixel dust masses with those for $>3\sigma$ pixel (Table 3), we find total dust masses of $(7.3 \pm 1.7) \times 10^5$ and $(8.3 \pm 2.1) \times 10^4$ $M_\odot$ for the LMC and SMC, respectively. For reference, the total gas masses that correspond to the same areas and same background removal as these total dust masses are 3.1×10^8 and 3.0×10^8 $M_\odot$ for the LMC and SMC, respectively.

Bot et al. (2010b) obtained global dust masses for both galaxies by fitting Draine et al. (2007) dust models to their global fluxes. They found masses of 3.6×10^6 and 0.29–1.1×10^6 $M_\odot$ for the LMC and SMC, respectively. Leroy et al. (2007b) fit the spatially resolved Spitzer observations with (Dale & Helou 2002) models and find a total SMC dust mass of 3×10^5 $M_\odot$. These values of the dust masses are factors of four to five larger than our values. The differences are likely due to different assumptions in the models used, the fitting techniques, the broader wavelength range of data, and/or the increased mixing of environments.

6.3. Total Gas-to-dust Ratios

One test of the submillimeter excess origin is to investigate how the overall gas-to-dust ratios for each model compare to the expected ratios. We explore overall gas-to-dust ratios as a

test of the consistency of each dust model with expectations based on the measured gas masses and metallicities of the LMC and SMC. The detailed spatial behavior of the gas-to-dust ratio with the environment is investigated in Roman-Duval et al. (2014).

The gas-to-dust ratios for each galaxy and all three models are given in Table 3. The dust masses are integrated over all the pixels that are detected at $>3\sigma$ in all observed bands. The total H gas masses given in the table footnote are integrated for the same pixels as the dust masses. The H I masses are directly from the H I measurements (Stanimirović et al. 2000; Muller et al. 2003; Kim et al. 2003) without any correction for opaque H I (Dickey et al. 2000; Fukui et al. 2014). The H$_2$ masses are computed from CO observations (Mizuno et al. 2001, 2006; Fukui et al. 2008; Wong et al. 2011) using $X_{CO} = 4.7 \times 10^{20}$ (Hughes et al. 2010) for the LMC and $X_{CO} = 6 \times 10^{21}$ (Leroy et al. 2007a) for the SMC. The appropriate X_{CO} to use is a matter of debate, but the expected range of this conversion factor is not large enough to strongly impact the total gas masses (Fukui & Kawamura 2010; Bolatto et al. 2013). The ratios given only include hydrogen, and thus are formally H gas-to-dust ratios, but for simplicity we refer to them as gas-to-dust ratios.

The range of reasonable gas-to-dust ratios can be estimated in three ways. The first scales the range of observed gas-to-dust ratios in the MW by the LMC and SMC metallicities. The second assumes the MW depletion factors and applies them to the measured LMC and SMC abundances. The third assumes that all the metals available are in the form of dust and this produces a minimum possible gas-to-dust ratio. The MW depletions and gas-to-dust ratios vary with environment and the global values in the Magellanic clouds will be some unknown mix of different ISM environments. As a result, we can only predict a possible range of gas-to-dust ratios.

The first method assumes that the relative amount of metals in the LMC and SMC dust is the same as the MW, but scaled in proportion to each galaxy's metallicity. Thus, the expected gas-to-dust ratio will be two times (LMC) and five times (SMC) the MW gas-to-dust ratio. The MW gas-to-dust ratio varies
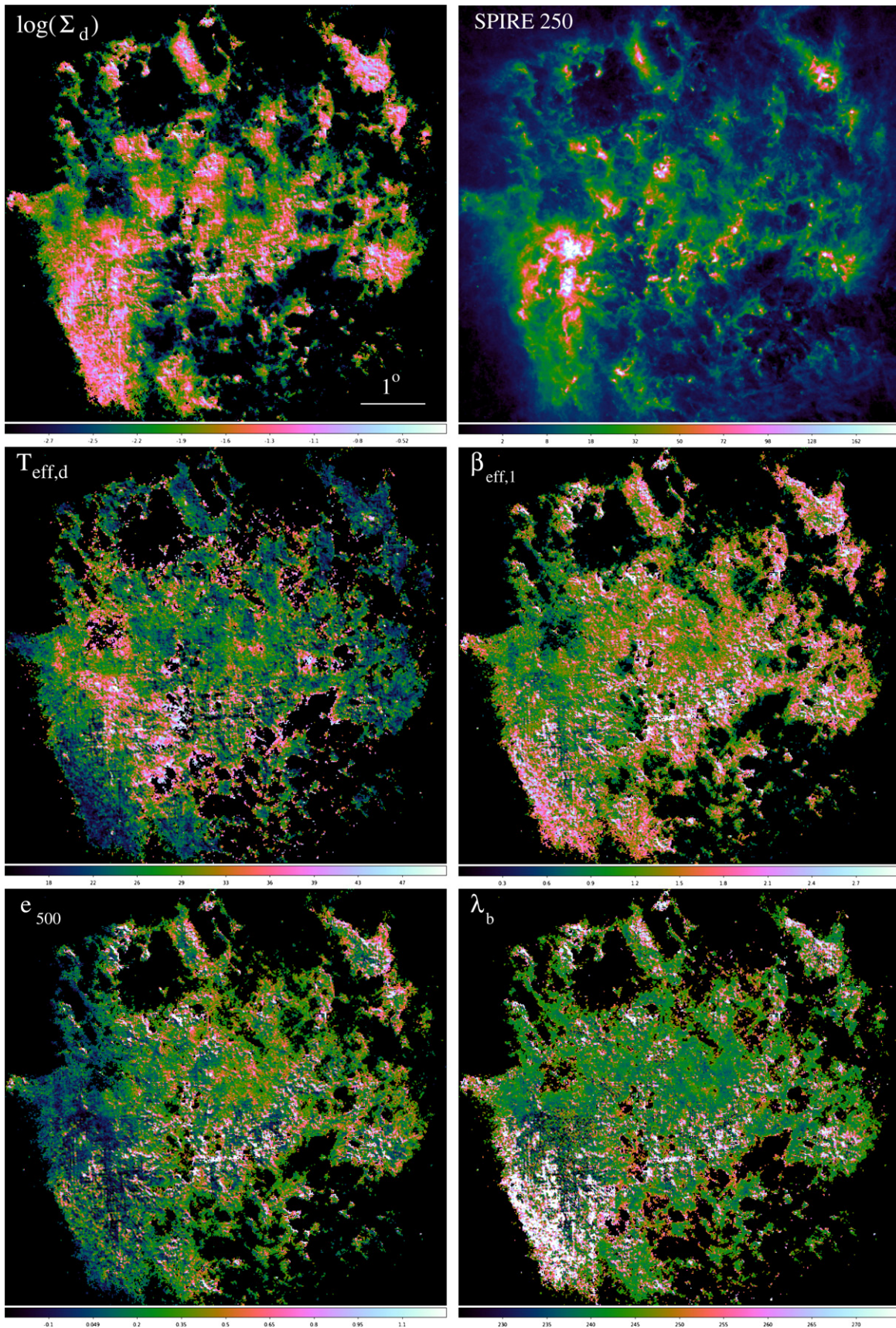
Figure 6. Spatial distribution of $\log(\Sigma_d)$, $T_{\mathrm{eff,d}}$, $\beta_{\mathrm{eff,1}}$, e_{500}, and λ_b for the BEMBB model are shown for the LMC using the expectation value for each pixel. In addition, the processed SPIRE 250 μm image (Section 2) is shown. The images are shown using the cubehelix color mapping (Green 2011). The left/right and up/down streaks seen are residual instrumental artifacts that are aligned along the PACS/SPIRE scan direction.

(A color version of this figure is available in the online journal.)
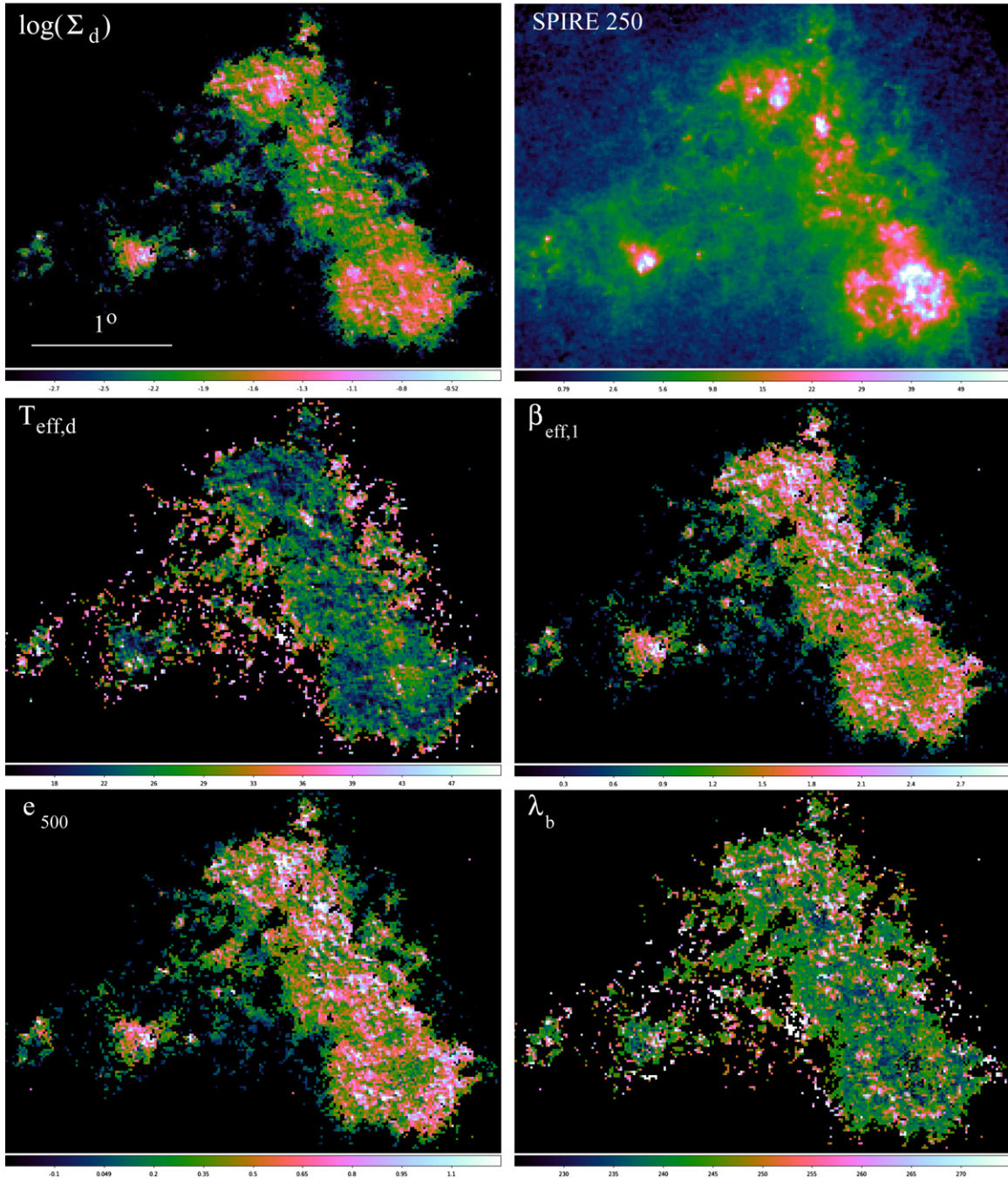
Figure 7. Spatial distribution of Σ_d, $T_{eff,d}$, $\beta_{eff,1}$, e_{500}, and λ_b for the BEMBB model are shown for the SMC using the "exp" value for each pixel. In addition, the processed SPIRE 250 μm image (Section 2) is shown. The images are shown using the cubehelix color mapping (Green 2011).
(A color version of this figure is available in the online journal.)

from $\sim$250 for the very diffuse ISM ($F_* = 0$) to $\sim$100 for the moderately dense ISM ($F_* = 1$) (Jenkins 2009). For the LMC, we therefore expect a gas-to-dust ratio between 200 to 500 while, for the SMC, we expect a gas-to-dust ratio between 500 and 1250. The second method assumes the MW depletion patterns (Jenkins 2009) and the measured LMC and SMC abundances for each element (Russell & Dopita 1992). The resulting expected LMC gas-to-dust ratios range between 150 to 360 and the expected SMC gas-to-dust ratios range between 540 to 1300. Combining the two different methods, the expected gas-to-dust ratios are 150–500 and 500–1300 for the LMC and SMC, respectively. Finally, the minimum allowed gas-to-dust ratio can

be computed by assuming all the metals in the ISM in the form of dust. Assuming the measured LMC and SMC abundances, this gives minimum gas-to-dust ratios of 105 and 300, respectively. These expected gas-to-dust ratios are given in Table 3.

The gas-to-dust ratios for all three models are plotted in Figure 5 along with the allowed ranges for reasonable depletions and maximum depletions. From Table 3 and this figure, it is clear that the TTMBB models give gas-to-dust ratios that are lower than even possible assuming that all the metals are present in the dust. The TTMBB model gives low gas-to-dust ratios because it requires large dust masses for the second cold component to be able to reproduce the observed submillimeter excess emission.
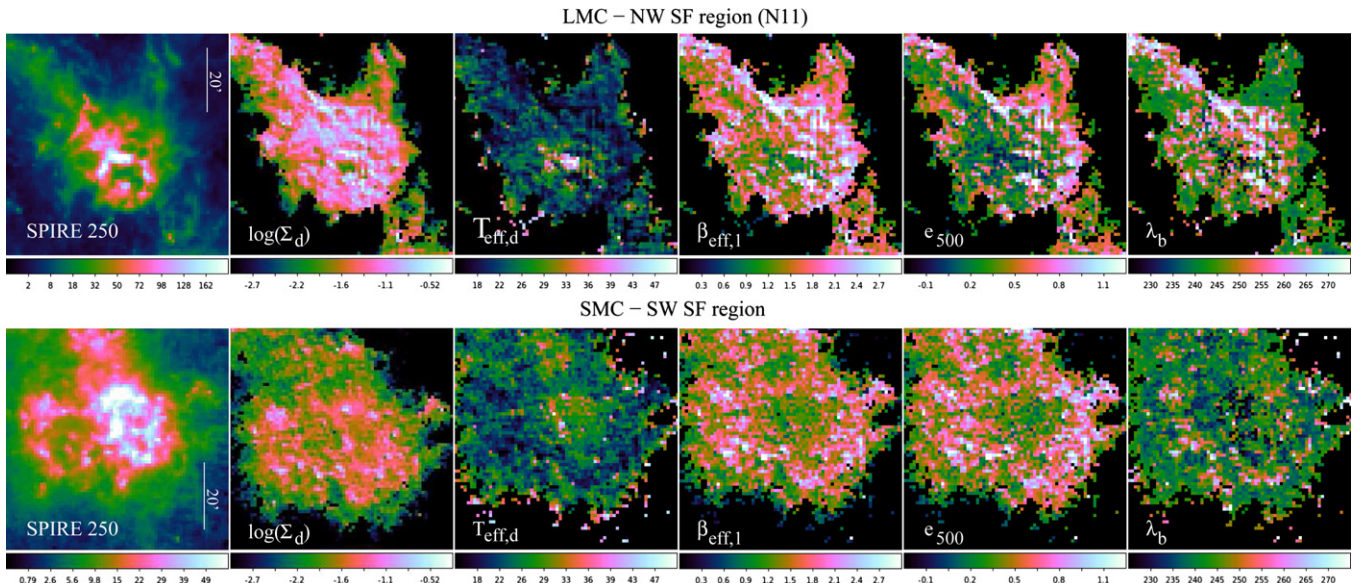
Figure 8. Spatial distribution of Σ_d, $T_{\mathrm{eff,d}}$, $\beta_{\mathrm{eff,1}}$, e_{500}, and λ_b for the BEMBB model are shown for one star-forming region each in the LMC and SMC using the "exp" value for each pixel. In addition, the processed SPIRE 250 μm images (Section 2) is shown. The images are shown using the cubehelix color mapping (Green 2011). (A color version of this figure is available in the online journal.)

Thus, the TTMBB model is not a reasonable model for the dust emission in the LMC or SMC. The SMBB and BEMBB models give similar gas-to-dust ratios for both galaxies. For the LMC, both models give ratios that are well within the reasonable range of values. For the SMC, these two models both give values that are above the reasonable values. This is an indication that the depletions in the SMC are lower than those the in MW or that the dust properties are different (e.g., a smaller $\kappa_{\mathrm{eff,160}}$ value than that assumed in this paper).

6.4. Spatial Variations

The spatial variations across both galaxies in the different fit parameters for the BEMBB model are shown in Figures 6 and 7. We only show the BEMBB results here because the evidence in the previous sections gives a fairly strong indication that the BEMBB fits the data best (Section 6.1) and provides a physically reasonable gas-to-dust ratio (Section 6.3). The maps of dust surface density (Σ_d) and temperature ($T_{\mathrm{eff,d}}$) show qualitatively similar behaviors to previous works (Bot et al. 2004; Leroy et al. 2007b; Bernard et al. 2008). In detail, our maps differ mainly in showing finer structure due to the higher spatial resolution *Herschel* observations. One illustration of this effect is that the peak $T_{\mathrm{eff,d}}$ in the 30 Dor region in our map is ∼60 K, significantly higher than the ∼35 K found by Bernard et al. (2008).

The higher spatial resolution of our maps does allow for detailed investigations of individual star-forming regions. This is illustrated by Figure 8 where cutouts of the BEMBB fit parameter maps for a star-forming region in each galaxy are shown. The morphology of these two star-forming regions is similar. The SPIRE 250 μm emission is strongly peaked in the region centers in contrast to the dust surface density which is more constant across the regions. This difference is caused by the center of these regions having high $T_{\mathrm{eff,d}}$ values. The β_{eff} and e_{500} maps of both regions have very similar morphologies, visually illustrating that these two fit parameters are strongly correlated. Finally, the λ_b images show coherent structures with fairly small variations overall. The submillimeter excess as parametrized by e_{500} is near zero in the center of the two star-

forming regions and rises rapidly to values around one near the edges. This behavior is intriguing, but the strong correlations of e_{500} with β_{eff} indicate that more work is needed to determine if this is real or due to noise induced correlations.

The overall properties of the global submillimeter excess between the LMC and SMC show trends that are consistent with previous work. The average LMC and SMC e_{500} values are 0.27 and 0.43 when the average is done using the "realize" method and each pixel has equal weight. This can be visually seen in the e_{500} images in Figures 6 and 7 where the SMC shows a higher filling factor of high e_{500} values than the LMC. This trend of the lower metallicity SMC having a higher submillimeter excess than the LMC is expected given the results from global studies of the submillimeter excess Rémy-Ruyer et al. (2013). A fairer comparison of the absolute value of e_{500} with global SED fits is the dust surface density weighted averages that are 0.11 and 0.26 for the LMC and SMC, respectively. Finally, the average values of λ_b are ∼240 for both types of averages and both galaxies. This wavelength is similar to that found by Li & Draine (2001) from fitting the DIRBE MW diffuse spectrum.

To investigate the variations in fit parameters more quantitatively, we plot all the correlations between the different fit parameters for the LMC in Figure 9. The plots for the SMC are very similar and are not shown. These plots show the density of points where each point represents a single pixel. The values used for each pixel use the "realize" method where the likelihood functions are randomly sampled once for each pixel. This means that these density plots statistically sample the full information for the fit from each pixel. Repeating the "realize" method process with a different random sampling for each pixel produces plots that are very similar. This indicates that these plots fully capture the correlations between fit parameters with a single sampling of each pixel's likelihood function due to the large number of pixels. Plots created using the "max" and "exp" methods are significantly different because they do not fully include the information on the uncertainties in the fits to each pixel. As an example of the difference between the different "best-fit" methods, a flat likelihood function would show a single value for "max" and "exp," while the "realize" method
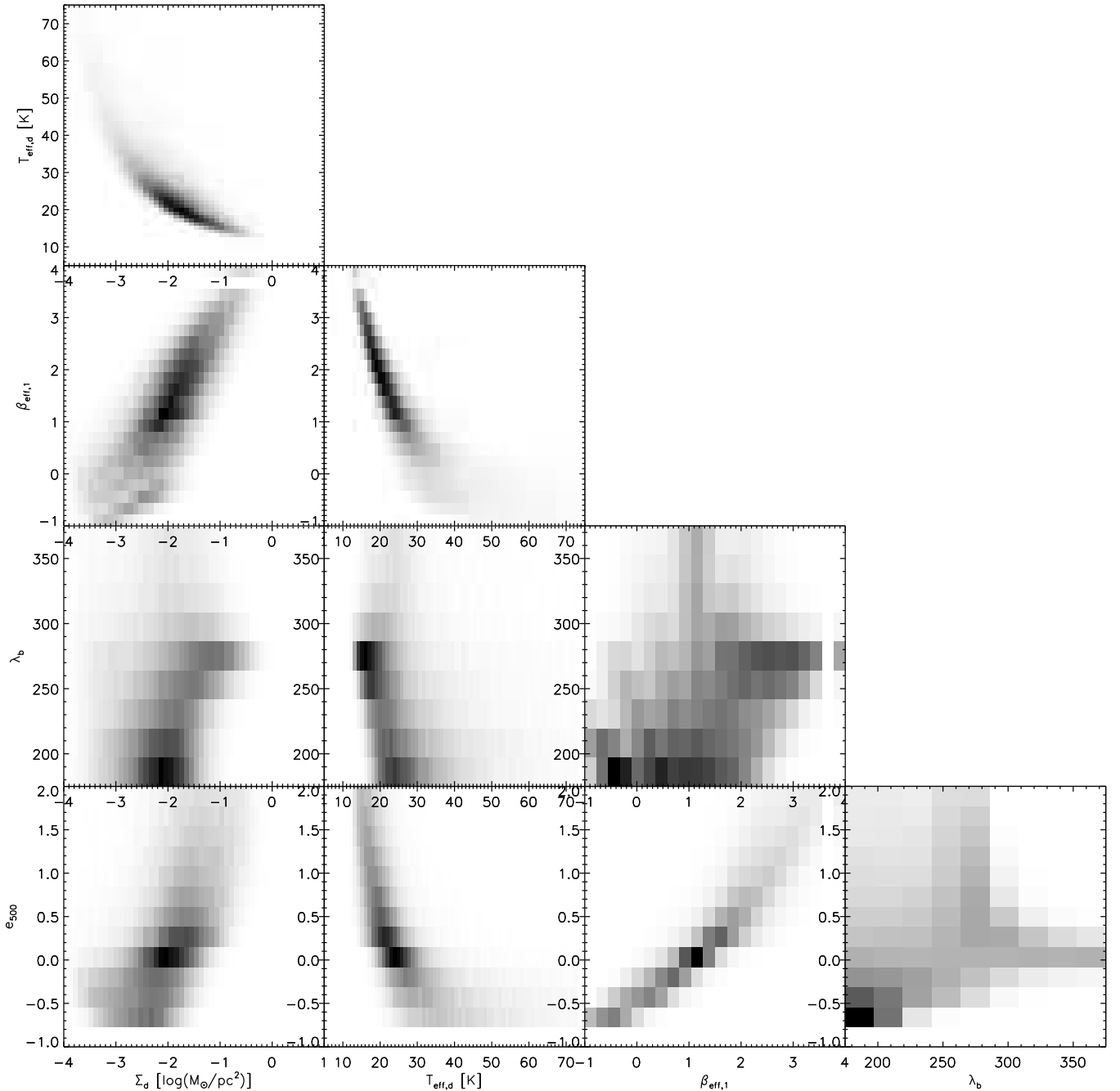
Figure 9. Correlations for the LMC between all five fit parameters for the BEMBB model are plotted. The plots are density plots where each point that contributes to the density is a single realization of the full likelihood function for a single pixel.

would have a value that was randomly distributed over the entire parameter range.

These plots show that many of the parameters are correlated with each other, sometimes quite strongly. The strongest correlations are seen between $\log(\Sigma_d)$ and $T_{\rm eff,d}$, $\log(\Sigma_d)$ and $\beta_{\rm eff,1}$, $T_{\rm eff,d}$ and $\beta_{\rm eff,1}$, and $\beta_{\rm eff,1}$ and e_{500}. The origin of these correlations can be either real or a result of interactions between noise in the measurements and model fit parameters. The correlation between $\log(\Sigma_d)$ and $T_{\rm eff,d}$ is real in that it reflects the detection thresholds of the HERITAGE data. Hotter dust can be more easily detected at lower dust surface densities than cooler dust due to the $T_{\rm eff,d}^4$ behavior of blackbodies. The anti-correlation between $T_{\rm eff,d}$ and $\beta_{\rm eff}$ is one of the correlations that has been studied extensively to learn if it is due to noise or real variations

in the dust properties (Dupac et al. 2003; Shetty et al. 2009a, 2009b; Galliano et al. 2011; Juvela & Ysard 2012; Kelly et al. 2012; Ysard et al. 2012; Veneziani et al. 2013). Laboratory data on dust analogs do show a shallow anti-correlation between $T_{\rm eff,d}$ and $\beta_{\rm eff}$ (Coupeaud et al. 2011), but noise in measurements also produces a similar or larger anti-correlation. Kelly et al. (2012) have proposed the use of a hierarchical Bayesian model to solve for the true $T_{\rm eff,d}$–$\beta_{\rm eff}$ correlation, where the hierarchical model assumes a single $T_{\rm eff,d}$ and $\beta_{\rm eff}$ with some distribution around these values. In fitting an entire galaxy, such an assumption is not justified because, for example, there are regions near star formation that will be significantly hotter than regions further away. In addition, Juvela et al. (2013) find there are biases in all the currently proposed methods for determining the true

$T_{\mathrm{eff,d}}-\beta_{\mathrm{eff}}$ relation. Thus, we choose to graphically display the correlations using the "realize" method and not explicitly fit for the correlation. In future work, we plan to incorporate additional observations of the ISM and physical models for the correlations between different ISM parameters (e.g., dust and gas surface densities).

Figure 9 shows the correlations between the submillimeter excess e_{500} and other dust properties. The value of e_{500} is positively correlated with Σ_d and $\beta_{\mathrm{eff,1}}$ and negatively correlated with $T_{\mathrm{eff,d}}$. This may be real or it may be due to the $T_{\mathrm{eff,d}}$ versus $\beta_{\mathrm{eff,1}}$ anti-correlation that is also very clearly seen. The positive correlation between e_{500} and Σ_d is the opposite of what was found by Galliano et al. (2011) for a pathfinder study using a portion of the HERITAGE data on the LMC and Paradis et al. (2012) for the MW. The difference between these works and our work may be due to changes in the PACS and SPIRE calibration, different fitting methods, and/or different dust emission models. Future work will investigate these differences by using the same data, same fitting code, and expanding the dust emission model to include more sophisticated dust emission models.

7. CONCLUSIONS AND FUTURE WORK

We find that the Magellanic clouds show a submillimeter excess in the *Herschel* HERITAGE observations with a spatial resolution of $\sim$10 pc. This submillimeter excess seen in the Magellanic clouds is more likely to be due to variations in the dust emissivity wavelength dependence than a second population of colder dust. This is based on the BEMBB model providing the best fit to the HERITAGE data and producing realistic gas-to-dust ratio values. The average submillimeter excesses seen at 500 μm at $\sim$10 pc resolution are 27% and 43% for the LMC and SMC, respectively. There are trends of the submillimeter excess and environment (probed by Σ_d and $T_{\mathrm{eff,d}}$), but the true nature of these trends will be investigated in future work that incorporates more data and more physical models of the ISM.

The total dust masses integrated over the pixels detected at 3σ in all five PACS/SPIRE bands using our favored model (BEMBB) are $(7.3 \pm 1.7) \times 10^5$ and $(8.3 \pm 2.1) \times 10^4$ $M_\odot$ for the LMC and SMC, respectively. These dust masses are significantly lower (factors of four to five) than would be expected from previous dust masses measurements (Leroy et al. 2007b; Bot et al. 2010b). The lower dust masses we derive have important implications for the study of the lifecycle of dust in the Magellanic clouds as the relative contributions between asymptotic giant branch stars, supernovae, and the ISM for the formation of dust change significantly (Matsuura et al. 2009; Boyer et al. 2012; Matsuura et al. 2013; Zhukovska & Henning 2013).

Future studies will focus on adding more physics to the fitting for dust properties. One rich area for future work will be to include constraints from other observations of the ISM in the Magellanic clouds. An initial foray into this area is the focus of Roman-Duval et al. (2014) who use the dust surface densities from this paper to investigate the dependence of the gas-to-dust ratio on environment. For the dust modeling, in particular, future work will include more sophisticated dust grain models (e.g., Weingartner & Draine 2001; Compiègne et al. 2011; Galliano et al. 2011) and shorter wavelength infrared observations (e.g., *Spitzer* IRAC/MIPS data) to better constrain the possible grain compositions.

REFERENCES

Aniano, G., Draine, B. T., Gordon, K. D., & Sandstrom, K. 2011, PASP, 123, 1218
Balog, Z., Müller, T., Nielbock, M., et al. 2013, ExA, 37, 129
Bendo, G. J., Griffin, M. J., Bock, J. J., et al. 2013, MNRAS, 433, 3062
Bernard, J.-P., Reach, W. T., Paradis, D., et al. 2008, AJ, 136, 919
Bianchi, S. 2013, A&A, 552, A89
Boggess, N. W., Mather, J. C., Weiss, R., et al. 1992, ApJ, 397, 420
Bolatto, A. D., Wolfire, M., & Leroy, A. K. 2013, ARA&A, 51, 207
Bot, C., Boulanger, F., Lagache, G., Cambrésy, L., & Egret, D. 2004, A&A, 423, 567
Bot, C., Rubio, M., Boulanger, F., et al. 2010a, A&A, 524, A52
Bot, C., Ysard, N., Paradis, D., et al. 2010b, A&A, 523, A20
Boudet, N., Mutschke, H., Nayral, C., et al. 2005, ApJ, 633, 272
Boyer, M. L., Srinivasan, S., Riebel, D., et al. 2012, ApJ, 748, 40
Clayton, G. C., & Martin, P. G. 1985, ApJ, 288, 558
Compiègne, M., Verstraete, L., Jones, A., et al. 2011, A&A, 525, A103
Coupeaud, A., Demyk, K., Meny, C., et al. 2011, A&A, 535, A124
Dale, D. A., Aniano, G., Engelbracht, C. W., et al. 2012, ApJ, 745, 95
Dale, D. A., & Helou, G. 2002, ApJ, 576, 159
Desert, F.-X., Boulanger, F., & Puget, J. L. 1990, A&A, 237, 215
Dickey, J. M., Mebold, U., Stanimirovic, S., & Staveley-Smith, L. 2000, ApJ, 536, 756
Draine, B. T., Aniano, G., Krause, O., et al. 2014, ApJ, 780, 172
Draine, B. T., Dale, D. A., Bendo, G., et al. 2007, ApJ, 663, 866
Draine, B. T., & Li, A. 2007, ApJ, 657, 810
Dupac, X., Bernard, J.-P., Boudet, N., et al. 2003, A&A, 404, L11
Fitzpatrick, E. L. 1985, ApJ, 299, 219
Fukui, Y., & Kawamura, A. 2010, ARA&A, 48, 547
Fukui, Y., Kawamura, A., Minamidani, T., et al. 2008, ApJS, 178, 56
Fukui, Y., Okamoto, R., Yamamoto, H., et al. 2014, ApJ, 796, 59
Galliano, F., Hony, S., Bernard, J.-P., et al. 2011, A&A, 536, A88
Galametz, M., Hony, S., Galliano, F., et al. 2013, MNRAS, 431, 1596
Galametz, M., Madden, S. C., Galliano, F., et al. 2011, A&A, 532, A56
Galliano, F., Madden, S. C., Jones, A. P., Wilson, C. D., & Bernard, J.-P. 2005, A&A, 434, 867
Galliano, F., Madden, S. C., Jones, A. P., et al. 2003, A&A, 407, 159
Gordon, K. D., & Clayton, G. C. 1998, ApJ, 500, 816
Gordon, K. D., Clayton, G. C., Misselt, K. A., Landolt, A. U., & Wolff, M. J. 2003, ApJ, 594, 279
Gordon, K. D., Galliano, F., Hony, S., et al. 2010, A&A, 518, L89
Gordon, K. D., Meixner, M., Meade, M. R., et al. 2011, AJ, 142, 102
Green, D. A. 2011, BASI, 39, 289
Griffin, M. J., Abergel, A., Abreu, A., et al. 2010, A&A, 518, L3
Griffin, M. J., North, C. E., Schulz, B., et al. 2013, MNRAS, 434, 992
Gut, A. 2009, An Intermediate Course in Probability, Springer Texts in Statistics (Berlin: Springer)
Herschel Space Observatory. 2011, SPIRE Observers Manual, Tech. Rep. HERSCHEL-DOC-0798, Version 2.4 (Noordwijk: ESA)
Hildebrand, R. H. 1983, QJRAS, 24, 267
Hilditch, R. W., Howarth, I. D., & Harries, T. J. 2005, MNRAS, 357, 304
Hughes, A., Wong, T., Ott, J., et al. 2010, MNRAS, 406, 2065
Israel, F. P., Wall, W. F., Raban, D., et al. 2010, A&A, 519, A67
Jager, C., Mutschke, H., & Henning, T. 1998, A&A, 332, 291
Jenkins, E. B. 2009, ApJ, 700, 1299
Juvela, M., Montillaud, J., Ysard, N., & Lunttila, T. 2013, A&A, 556, A63
Juvela, M., & Ysard, N. 2012, A&A, 541, A33
Kelly, B. C., Shetty, R., Stutz, A. M., et al. 2012, ApJ, 752, 55
Kessler, M. F., Steinz, J. A., Anderegg, M. E., et al. 1996, A&A, 315, L27
Kim, S., Staveley-Smith, L., Dopita, M. A., et al. 2003, ApJS, 148, 473
Kirkpatrick, A., Calzetti, D., Galametz, M., et al. 2013, ApJ, 778, 51
Lequeux, J., Maurice, E., Prevot-Burnichon, M.-L., Prevot, L., & Rocca-Volmerange, B. 1982, A&A, 113, L15
Leroy, A., Bolatto, A., Stanimirovic, S., et al. 2007a, ApJ, 658, 1027
Leroy, A., Cannon, J., Walter, F., Bolatto, A., & Weiss, A. 2007b, ApJ, 663, 990
Li, A., & Draine, B. T. 2001, ApJ, 554, 778
Maíz Apellániz, J., & Rubio, M. 2012, A&A, 541, A54

Mather, J. C., Fixsen, D. J., & Shafer, R. A. 1993, Proc. SPIE, 2019, 168
Mathis, J. S., Rumpl, W., & Nordsieck, K. H. 1977, ApJ, 217, 425
Matsuura, M., Barlow, M. J., Zijlstra, A. A., et al. 2009, MNRAS, 396, 918
Matsuura, M., Woods, P. M., & Owen, P. J. 2013, MNRAS, 429, 2527
Meixner, M., Galliano, F., Hony, S., et al. 2010, A&A, 518, L71
Meixner, M., Gordon, K. D., Indebetouw, R., et al. 2006, AJ, 132, 2268
Meixner, M., Panuzzo, P., Roman-Duval, J., et al. 2013, AJ, 146, 62
Mennella, V., Brucato, J. R., Colangeli, L., et al. 1998, ApJ, 496, 1058
Mennella, V., Colangeli, L., & Bussoletti, E. 1995, A&A, 295, 165
Misselt, K. A., Clayton, G. C., & Gordon, K. D. 1999, ApJ, 515, 128
Mizuno, N., Muller, E., Maeda, H., et al. 2006, ApJL, 643, L107
Mizuno, N., Rubio, M., Mizuno, A., et al. 2001, PASJ, 53, L45
Muller, E., Staveley-Smith, L., Zealey, W., & Stanimirović, S. 2003, MNRAS, 339, 105
Müller, T., Nielbock, M., Balog, Z., Klaas, U., & Vilenius, E. 2011a, PACS Photometer—Point-Source Flux Calibration, Tech. Rep. PICC-ME-TN-037, Herschel
Müller, T., Okumura, K., & Klaas, U. 2011b, PACS Photometer Passbands and Colour Correction Factors for Various Source SEDs, Tech. Rep. PICC-ME-TN-038, Herschel
Paradis, D., Bernard, J., & Mény, C. 2009, A&A, 506, 745
Paradis, D., Paladini, R., Noriega-Crespo, A., et al. 2012, A&A, 537, A113
Peimbert, A., & Peimbert, M. 2010, ApJ, 724, 791
Pilbratt, G. L., Riedinger, J. R., Passvogel, T., et al. 2010, A&A, 518, L1
Planck Collaboration, Ade, P. A. R., Aghanim, N., et al. 2011, A&A, 536, A17
Poglitsch, A., Waelkens, C., Geis, N., et al. 2010, A&A, 518, L2
Prevot, M. L., Lequeux, J., Prevot, L., Maurice, E., & Rocca-Volmerange, B. 1984, A&A, 132, 389
Reach, W. T., Dwek, E., Fixsen, D. J., et al. 1995, ApJ, 451, 188
Rémy-Ruyer, A., Madden, S. C., Galliano, F., et al. 2013, A&A, 557, A95
Roman-Duval, J., Gordon, K. D., Meixner, M., et al. 2014, ApJ, 797, 86
Roth, K. C., & Blades, J. C. 1997, ApJL, 474, L95
Russell, S. C., & Dopita, M. A. 1992, ApJ, 384, 508

Schwering, P. B. W. 1989, A&AS, 79, 105
Schwering, P. B. W., & Israel, F. P. 1989, A&AS, 79, 79
Shetty, R., Kauffmann, J., Schnee, S., & Goodman, A. A. 2009a, ApJ, 696, 676
Shetty, R., Kauffmann, J., Schnee, S., Goodman, A. A., & Ercolano, B. 2009b, ApJ, 696, 2234
Skibba, R. A., Engelbracht, C. W., Aniano, G., et al. 2012, ApJ, 761, 42
Sofia, U. J., Gordon, K. D., Clayton, G. C., et al. 2006, ApJ, 636, 753
Stanimirović, S., Staveley-Smith, L., van der Hulst, J. M., et al. 2000, MNRAS, 315, 791
Staveley-Smith, L., Kim, S., Calabretta, M. R., Haynes, R. F., & Kesteven, M. J. 2003, MNRAS, 339, 87
Valencic, L. A., Clayton, G. C., & Gordon, K. D. 2004, ApJ, 616, 912
Valencic, L. A., Clayton, G. C., Gordon, K. D., & Smith, T. L. 2003, ApJ, 598, 369
Veneziani, M., Piacentini, F., Noriega-Crespo, A., et al. 2013, ApJ, 772, 56
Walker, A. R. 2012, Ap&SS, 341, 43
Weingartner, J. C., & Draine, B. T. 2001, ApJ, 548, 296
Welty, D. E., & Crowther, P. A. 2010, MNRAS, 404, 1321
Welty, D. E., Lauroesch, J. T., Blades, J. C., Hobbs, L. M., & York, D. G. 1997, ApJ, 489, 672
Welty, D. E., Lauroesch, J. T., Blades, J. C., Hobbs, L. M., & York, D. G. 2001, ApJL, 554, L75
Werner, M. W., Roellig, T. L., Low, F. J., et al. 2004, ApJS, 154, 1
Wong, T., Hughes, A., Ott, J., et al. 2011, ApJS, 197, 16
Wright, E. L., Mather, J. C., Bennett, C. L., et al. 1991, ApJ, 381, 200
Ysard, N., Juvela, M., Demyk, K., et al. 2012, A&A, 542, A21
Zhukovska, S., & Henning, T. 2013, A&A, 555, A99
Zubko, V., Dwek, E., & Arendt, R. G. 2004, ApJS, 152, 211
Zubko, V. G., Mennella, V., Colangeli, L., & Bussoletti, E. 1996, MNRAS, 282, 1321

Erratum: "Dust and Gas in the Magellanic Clouds from the HERITAGE *Herschel* Key Project. I. Dust Properties and Insights into the Origin of the Submm Excess Emission" (2014, ApJ, 797, 85)

Karl D. Gordon[1,2], Julia Roman-Duval[1], Caroline Bot[3], Margaret Meixner[1], Brian Babler[4], Jean-Philippe Bernard[5,6],
Alberto Bolatto[7], Martha L. Boyer[8,9], Geoffrey C. Clayton[10], Charles Engelbracht[11,12], Yasuo Fukui[13], Maud Galametz[14],
Frederic Galliano[15], Sacha Hony[15], Annie Hughes[16], Remy Indebetouw[17], Frank P. Israel[18], Katie Jameson[7], Akiko Kawamura[19],
Vianney Lebouteiller[15], Aigen Li[20], Suzanne C. Madden[15], Mikako Matsuura[21], Karl Misselt[11], Edward Montiel[10,11],
K. Okumura[15], Toshikazu Onishi[22], Pasquale Panuzzo[15,23], Deborah Paradis[5,6], Monica Rubio[24], Karin Sandstrom[11],
Marc Sauvage[15], Jonathan Seale[1,25], Marta Sewiło[25], Kirill Tchernyshyov[25], and Ramin Skibba[11,26]
[1] Space Telescope Science Institute, 3700 San Martin Drive, Baltimore, MD 21218, USA
[2] Sterrenkundig Observatorium, Universiteit Gent, Gent, Belgium
[3] Observatoire astronomique de Strasbourg, Université de Strasbourg, CNRS, UMR 7550, 11 rue de l Université, F-67000 Strasbourg, France
[4] Department of Astronomy, 475 North Charter Street, University of Wisconsin, Madison, WI 53706, USA
[5] CESR, Université de Toulouse, UPS, 9 Avenue du Colonel Roche, F-31028 Toulouse, Cedex 4, France
[6] Université de Toulouse, UPS-OMP, IRAP, 31028 Toulouse Cedex 4, France
[7] Department of Astronomy, Lab for Millimeter-wave Astronomy, University of Maryland, College Park, MD 20742, USA
[8] Observational Cosmology Lab, Code 665, NASA Goddard Space Flight Center, Greenbelt, MD 20771, USA
[9] Oak Ridge Associated Universities (ORAU), Oak Ridge, TN 37831, USA
[10] Louisiana State University, Department of Physics & Astronomy, 233-A Nicholson Hall, Tower Dr., Baton Rouge, LA 70803, USA
[11] Steward Observatory, University of Arizona, 933 North Cherry Avenue, Tucson, AZ 85721, USA
[12] Raytheon Company, 1151 East Hermans Road, Tucson, AZ 85756, USA
[13] Department of Physics, Nagoya University, Furo-cho, Chikusa-ku, Nagoya 464-8602, Japan
[14] European Southern Observatory, Karl-Schwarzschild-Str. 2, D-85748 Garching-bei-Mnchen, Germany
[15] CEA, Laboratoire AIM, Irfu/SAp, Orme des Merisiers, F-91191 Gif-sur-Yvette, France
[16] Max-Planck-Institut für Astronomie, Königstuhl 17, D-69117 Heidelberg, Germany
[17] Department of Astronomy, University of Virginia, and National Radio Astronomy Observatory, 520 Edgemont Road, Charlottesville, VA 22903, USA
[18] Sterrewacht Leiden, Leiden University, P.O. Box 9513, NL-2300 RA Leiden, The Netherlands
[19] National Astronomical Observatory of Japan, Osawa, Mitaka, Tokyo, 181-8588, Japan
[20] 314 Physics Building, Department of Physics and Astronomy, University of Missouri, Columbia, MO 65211, USA
[21] Department of Physics and Astronomy, University College London, Gower Street, London WC1E 6BT, UK
[22] Department of Astrophysics, Graduate School of Science, Osaka Prefecture University, Sakai, Osaka 599-8531, Japan
[23] CNRS, Observatoire de Paris—Lab. GEPI, Bat. 11, 5, place Jules Janssen, 92195 Meudon CEDEX, France
[24] Departamento de Astronomía, Universidad de Chile, Casilla 36-D, Santiago, Chile
[25] The Johns Hopkins University, Department of Physics and Astronomy, 366 Bloomberg Center, 3400 N. Charles Street, Baltimore, MD 21218, USA
[26] Center for Astrophysics and Space Sciences, Department of Physics, University of California, 9500 Gilman Dr, La Jolla, San Diego, CA 92093, USA
Received 2017 February 10; published 2017 March 7

The values of $\kappa_{\mathrm{eff},160}$ given in the original paper are missing a factor of π. This is because the routine used to compute $B_\lambda(T)$ was the IDL Astronomer User's Library[27] `planck.pro` and it returns $\pi B_\lambda(T)$. While this is explicitly documented in the `planck.pro` function, it was not realized by the first author until after the paper was published. This does not impact the results or conclusions of the paper as the values of $\kappa_{\mathrm{eff},160}$ used were determined based on fitting Milky Way observations using the same code that was used to fit the Magellanic Cloud observations. Thus, the correct values of $\kappa_{\mathrm{eff},160}$ are a factor of π larger than the ones quoted in the paper. Using Equation (5) from the paper with the values of $\kappa_{\mathrm{eff},160}$ given in the corrected Table 2 will reproduce the dust surface density result from the paper. The detailed fit parameter maps used in the paper are available online.[28]

The correct values of $\kappa_{\mathrm{eff},160}$ are approximately a factor of two larger than the values calculated from full dust grain models and discussed in Section 5.3 of the paper. This difference may be due to the simple models in our paper, which did not include the full physical treatment (e.g., multiple grain sizes/compositions with different temperatures) or, less likely, some issues with the assumptions in the dust grain models. We are carrying out work to investigate such issues for the dust in the Magellanic Clouds (and Milky Way) using more complicated dust grain models and additional observations. This work will be discussed in future papers.

There was a typo in Equation (4) with a factor of π missing from the denominator. This does not affect Equation (5) as it was derived correctly including this factor of π. The correct equation is

$$S_\lambda = \frac{\Sigma_d}{\frac{4}{3}\pi a^3 \rho} \pi a^2 Q_\lambda B_\lambda(T_d). \tag{4}$$

Last, there was a typo in Equation (15). The correct equation is

$$S_{\mathrm{band}} = \frac{\int S_\nu R_E(\nu)\,d\nu}{\int (\nu_o/\nu) R_E(\nu)\,d\nu}. \tag{15}$$

[27] https://idlastro.gsfc.nasa.gov/
[28] http://www.stsci.edu/~kgordon/magclouds_results/

Table 2
MW Diffuse Fit Results

Model	$\kappa_{\mathrm{eff},160}$[a] [cm^2 g^{-1}]	Other Parameters	Expectation Values
SMBB	$30.2 \pm 1.3 \pm 2.5$	$(T_{\mathrm{eff,d}}, \beta_{\mathrm{eff}})$	$(17.2 \pm 0.4$ K, $1.96 \pm 0.10)$
BEMBB	$36.4 \pm 4.7 \pm 2.5$	$(T_{\mathrm{eff,d}}, \beta_{\mathrm{eff,1}}, \lambda_b, e_{500})$	$(16.8 \pm 0.6$ K, $2.27 \pm 0.15, 294 \pm 29~\mu\mathrm{m}, 0.48 \pm 0.11)$
TTMBB	$1620 \pm 672 \pm 2.5$	$(T_{\mathrm{eff},d1}, T_{\mathrm{eff},d2}, \beta_{\mathrm{eff}}, e_{500})$	$(15.0 \pm 0.7$ K, 6.0 ± 0.8 K, $2.9 \pm 0.1, 0.91 \pm 0.25)$
TTMBB	$30.2 \pm 1.3 \pm 2.5$	adopted	

Note.
[a] The results are given as value $\pm$ fitting uncertainty $\pm$ systematic uncertainty.